Sedimentary Geology 407 (2020) 105737

Contents lists available at ScienceDirect

Sedimentary Geology

journal homepage: www.elsevier.com/locate/sedgeo

The Late Pleistocene-Holocene sedimentary evolution of the Sines Contourite Drift (SW Portuguese Margin): A multiproxy approach

Manuel Teixeira [a,b,c,*], Pedro Terrinha [a,b,c], Cristina Roque [a,d], Antje H.L. Voelker [e,f], Pedro Silva [a,g], Emília Salgueiro [e,f], Fátima Abrantes [e,f], Filipa Naughton [e,f], Anxo Mena [h], Gemma Ercilla [i], David Casas [i]

[a] IDL (Laboratório Associado) – Instituto Dom Luíz, Faculdade de Ciências da Universidade de Lisboa, Campo Grande, Edifício C1, 1749-016 Lisboa, Portugal
[b] Departamento de Geologia, Faculdade de Ciências da Universidade de Lisboa, Campo Grande, Edifício C6, 1749-016 Lisboa, Portugal
[c] IPMA – Instituto Português do Mar e da Atmosfera, Divisão de Geologia Marinha e Georecursos Marinhos, Rua C do Aeroporto, 1749-077 Lisboa, Portugal
[d] EMEPC – Estrutura de Missão para a Extensão da Plataforma Continental, Paço de Arcos, Portugal
[e] Divisão de Geologia Marinha e Georecursos Marinhos, Instituto Português do Mar e da Atmosfera (IPMA), Avenida Dr. Alfredo Magalhães Ramalho 6, 1495-165 Algés, Portugal
[f] Centro de Ciências Marinhas (CCMAR), Universidade do Algarve, Campus de Gambelas, 8005-139 Faro, Portugal
[g] IPL, ISEL – Instituto Superior de Engenharia de Lisboa, Physics Department, Lisboa, Portugal
[h] Dpt. Xeociencias Mariñas e O. T. Facultade de Ciências do Mar, Universidade de Vigo, Avenida das Abelleiras s/n, 36910 Vigo, Spain
[i] CSIC, Instituto de Ciencias del Mar, GMC, Passeig Marítim de la Barceloneta 37-49, E-08003 Barcelona, Spain

ARTICLE INFO

Article history:
Received 29 May 2020
Received in revised form 28 July 2020
Accepted 30 July 2020
Available online 5 August 2020

Editor: Dr. Jasper Knight

Keywords:
Sines Contourite Drift
Sediment properties
Late Pleistocene-Holocene
Mediterranean Outflow Water
Climate variations

ABSTRACT

The Sines Contourite Drift (SCD), located in the Alentejo margin, southwest Iberian continental margin, has been through many depositional phases in result of climatic variations and bottom current oscillations, which determined a variable depositional pattern and an irregular sedimentary evolution since the Late Pleistocene. The SCD, being in the main path of the Mediterranean Outflow Water (MOW), which greatly constrains the sedimentary building of this drift, constitutes the distal part of the Gulf of Cadiz Contourite Depositional System and its sedimentary evolution therefore reflects the history of MOW variations.

In order to investigate this, we report on a multiproxy analysis of grain-size, carbon content and physical, geochemical, and environmental-magnetic properties on the AMS ^{14}C dated 350-cm long gravity core CO14-GC-07, retrieved in the SCD, at 1425 meters water depth (mwd). The main objective is to reconstruct the evolution of the sedimentary package of the SCD from >43 cal kyr BP to Present and bring new insights about the impact of bottom currents' activity on the morphosedimentary evolution of the margin. Results show the existence of four distinct depositional phases in response to climate variations and bottom current oscillations during the Late Pleistocene-Holocene. Phase 1 (350–322 cm: >42.9 cal kyr BP) occurred in Marine Isotope Stage (MIS) 3 and presents silty-muddy sediments with presence of shell fragments and moderate bioturbation. Phase 2 (322–176 cm: >42.9–~30.5 cal kyr BP), which lasted from middle MIS 3 to the onset of MIS 2, reveals sediment coarsening towards the top limit, suggesting climate cooling and strong bottom current winnowing. Phase 3 (176–144 cm: ~30.5–17.1 cal kyr BP) covers most of MIS 2 prior to the last deglaciation and shows the sharpest variations on all sediment properties and the coarsest sediment facies, with Fe-rich layers associated with the increase of terrigenous input and sea-level regression that coincide with the enhancement of MOW. Phase 4 (144–0 cm: <17.1 cal kyr BP) is associated with the deglacial sea-level rise and represents a calmer depositional environment with finer sediments and increasing contributions of biogenic material. The MOW is the most prominent bottom current and the most active seabed shaping agent in the study area, whose vertical shifting during glacial (~800–2200 mwd) and interglacial (600–1500 mwd) periods is coincident with the most active morphosedimentary sector of the area, contributing to the development of landslide scars and sediment waves.

1. Introduction

Sediment properties allow for the understanding of the origin, environmental conditions, and the sedimentary evolution of sediment deposits (e.g., Baas et al., 1997; Abrantes et al., 1998; Silva et al., 2020). Along continental margins, where contourite drifts are generally formed, such sedimentary properties are particularly important, since

* Corresponding author at: IDL (Laboratório Associado) – Instituto Dom Luíz, Faculdade de Ciências da Universidade de Lisboa, Campo Grande, Edifício C1, 1749-016 Lisboa, Portugal.
E-mail address: macteixeira@fc.ul.pt (M. Teixeira).

https://doi.org/10.1016/j.sedgeo.2020.105737
0037-0738/

it allows the inference of events and processes associated with bottom current activity and contourite deposition (e.g., Faugères and Stow, 1993; Stow and Faugères, 2008). Contourite drifts are thus privileged records for palaeoclimate and palaeoceanographic reconstruction (e.g., Venuti et al., 2007; Knutz, 2008; Rebesco et al., 2014). Their stacking pattern allows inference of bottom current variability (e.g., Llave et al., 2001; Hernández-Molina et al., 2002), while sediment properties and microfossil content record evidence bottom current behaviour (Schönfeld and Zahn, 2000) associated with climate (Rogerson et al., 2005; Bahr et al., 2014; Kaboth et al., 2016; Kaboth et al., 2017a, 2017b).

Contourite deposits are commonly ascribed to bottom current activity, whose intensification generally leads to the formation of coarse deposits (Cacho et al., 2000; Llave et al., 2006; Voelker et al., 2006; Llave et al., 2007; Toucanne et al., 2007; Ercilla et al., 2016; Juan et al., 2016) during colder events (e.g., Schönfeld and Zahn, 2000; Rogerson et al., 2005; Llave et al., 2006) such as the Last Glacial Maximum (LGM), the Younger Dryas and Heinrich Events (HE), due to deposition and reworking of coarser material along the upper- (Llave et al., 2006; Toucanne et al., 2007) and middle continental slopes (Rogerson et al., 2005; Voelker et al., 2006; Rey et al., 2014; Bahr et al., 2015; Mena et al., 2018).

The Gulf of Cadiz Contourite Depositional System extends from the Gulf of Cadiz into the SW Portuguese margin, where the Sines Contourite Drift (SCD) has been formed (Fig. 1) (Hernández-Molina et al., 2003, 2011; Roque et al., 2015; Llave et al., 2019), mainly due to the action of the Mediterranean Outflow Water (MOW). This contourite depositional system has been studied during the last 40 years with particular attention to the Guadalquivir, Huelva, Faro, Albufeira, Portimão and Sagres drifts (e.g., Faugères et al., 1984; Gonthier et al., 1984; Nelson et al., 1993; Hernández-Molina et al., 2003, 2006; Llave et al., 2006, 2007; Hernández-Molina et al., 2011; Roque et al., 2012; Alonso et al., 2016; Hernández-Molina et al., 2016), aiming to understand the main depositional pattern through seismic and sediment proxy analyses from million-year to hundreds of thousand-year time scales. Time-series reconstructions have been made for this contourite depositional system, based on geochemical and faunal proxy data (Voelker et al., 2006). However, to better understand the sedimentary evolution of this contourite system at a millennial scale a broad multiproxy analysis should be done, to trace the impact and behaviour of MOW during the contouritic building process.

The SCD is a plastered drift (Hernández-Molina et al., 2011; Rodrigues, 2017), i.e., a giant and elongated drift (Faugères et al., 1999), whose evolution is greatly dependent on MOW's contour current activity, and its variability is strongly associated with climate change (e.g., Baas et al., 1997; Schönfeld and Zahn, 2000; Abrantes, 2016). The SCD sediments at the present-day are found at the interface between the MOW and the NADW (North Atlantic Deep Water), whose evolution led to distinctive coarse sediment layers, due to the stronger erosional and depositional capacities of an enhanced MOW outflow (e.g., Schönfeld and Zahn, 2000; Rogerson et al., 2005; Voelker et al., 2006; Toucanne et al., 2007), and to the development of slope instability (Roque et al., 2015; Teixeira et al., 2019). Mass wasting commonly appears associated with contourite deposits, both in glacial and non-glacial environments (Laberg and Camerlenghi, 2008; Ducassou et al., 2016). The presence of the SCD along the MOW's path significantly contributes to the formation of both slope instability at very low (<1°) slope angles, and sediment wave fields, whose discontinuities increase the development of landslide scars (Teixeira et al., 2019). Until now, the SCD remains the least known drift of the Gulf of Cadiz Contourite Depositional System, and despite the general information from IODP site U1391 (Stow et al., 2013), little is known about the Quaternary-Holocene sedimentary record of this contourite drift.

Therefore, this work presents a multiproxy characterization of the Sines Drift sediments, based on the analysis of the sedimentological, physical, geochemical, and environmental magnetic properties of a AMS ^{14}C dated sedimentary sequence, aiming to: i) to decode and understand the sedimentary evolution of the SCD at the millennial scale, during the Late Pleistocene to Holocene, ii) to infer the variability of the MOW during this time interval, and iii) to investigate the role of the interface MOW–NADW in shaping the middle slope morphology of the Alentejo Margin.

2. Geological and oceanographic setting

The Alentejo Margin is located in the West Iberian Margin, which was formed as a consequence of the breaking up of Pangaea during Triassic (Terrinha et al., 2019a) and subsequent Mesozoic rifting (Boillot et al., 1989; Pinheiro et al., 1996) that led to break-up during the Early Cretaceous (e.g., Terrinha et al., 2003). During Pliocene-Quaternary times, the SW Iberian Margin was subject to WNW-ESE oriented horizontal compression that favoured fault reactivation as evinced by offshore extensive seismicity (Terrinha et al., 2019b).

Contouritic deposition is dominant along the middle continental slope in the Alentejo Margin, forming the SCD, whose onset was in the Late Miocene (Hernández-Molina et al., 2013, 2014b; Stow et al., 2013; Rodrigues, 2017), experiencing a sedimentation rate of ~27 cm kyr^{-1} since the early Pleistocene (Stow et al., 2013).

A recent morphosedimentary study of the SCD (Teixeira et al., 2019) indicates that the SCD is affected by N-S to NE-SW crest-oriented sediment waves between ~800 and ~1700 mwd, at the interface of MOW/ENACW (Eastern North Atlantic Central Water), and by numerous landslide scars and gullies (Fig. 1) formed as consequence of gravity-driven activity (Roque et al., 2015; Teixeira et al., 2019). Landslides occur most regularly on steeper slopes especially in the vicinity of the Pereira de Sousa Fault scarp and bottom current-related features – e.g., moat, a trench carved by the action of bottom currents activity, but also on gentle slopes. Most of the landslide deposits developed in the continental slope accumulate at the base of the Pereira de Sousa Fault, in the Lebre Basin (Teixeira et al., 2019) (Fig. 1).

The oceanographic conditions in the Alentejo Margin (Fig. 1B) are driven by the circulation of superficial, intermediate and deep-water masses (e.g., Hernández-Molina et al., 2011). The superficial water masses circulation is essentially dominated by the North Atlantic Current (NAC) in the upper 100 mwd and by the underlying ENACW (Pollard et al., 1996), which circulates down to 600 mwd (van Aken, 2000a). At intermediate depths, roughly between ~600 and ~1500 mwd, MOW circulation is most effective in shaping the seabed. It flows northwards splitting into two main branches (Ambar and Howe, 1979; Hernández-Molina et al., 2011): the upper branch flowing between ~600 and 950 mwd (Cherubin et al., 2000; Serra and Ambar, 2002); the lower branch circulating roughly between ~1000–1500 mwd (e.g., Zenk and Armi, 1990; Serra and Ambar, 2002). Beneath these depths, deep circulation comprises the Labrador Sea Water between 1500 and 2200 mwd (Talley and McCartney, 1982), the NADW between 2200 and 4000 mwd (Caralp, 1988) and the Lower Deep Water, below 4000 mwd as part of the Antarctic Bottom Water (van Aken, 2000b). Thus, the significant bottom current activity in this region (Schönfeld and Zahn, 2000; Hernández-Molina et al., 2011, 2014b) controls the Alentejo Margin's morphosedimentary evolution, through the interplay with pre-existing tectonic structures and the interaction with seabed sediments (Teixeira et al., 2019).

3. Materials and methods

High-resolution multibeam swath bathymetry, multichannel seismic and sub-bottom profile data were used in this work for the morphologic and acoustic analysis of the core site area. Sediments from gravity-core CO14-GC-07 (37°27N, 09°32W, 1425 mwd) in the western boundary of the SCD were analysed through grain-size, carbonate content, physical and geochemical properties, and magnetic fabric. The core chronology was constructed based on six AMS ^{14}C dates (Table 1).

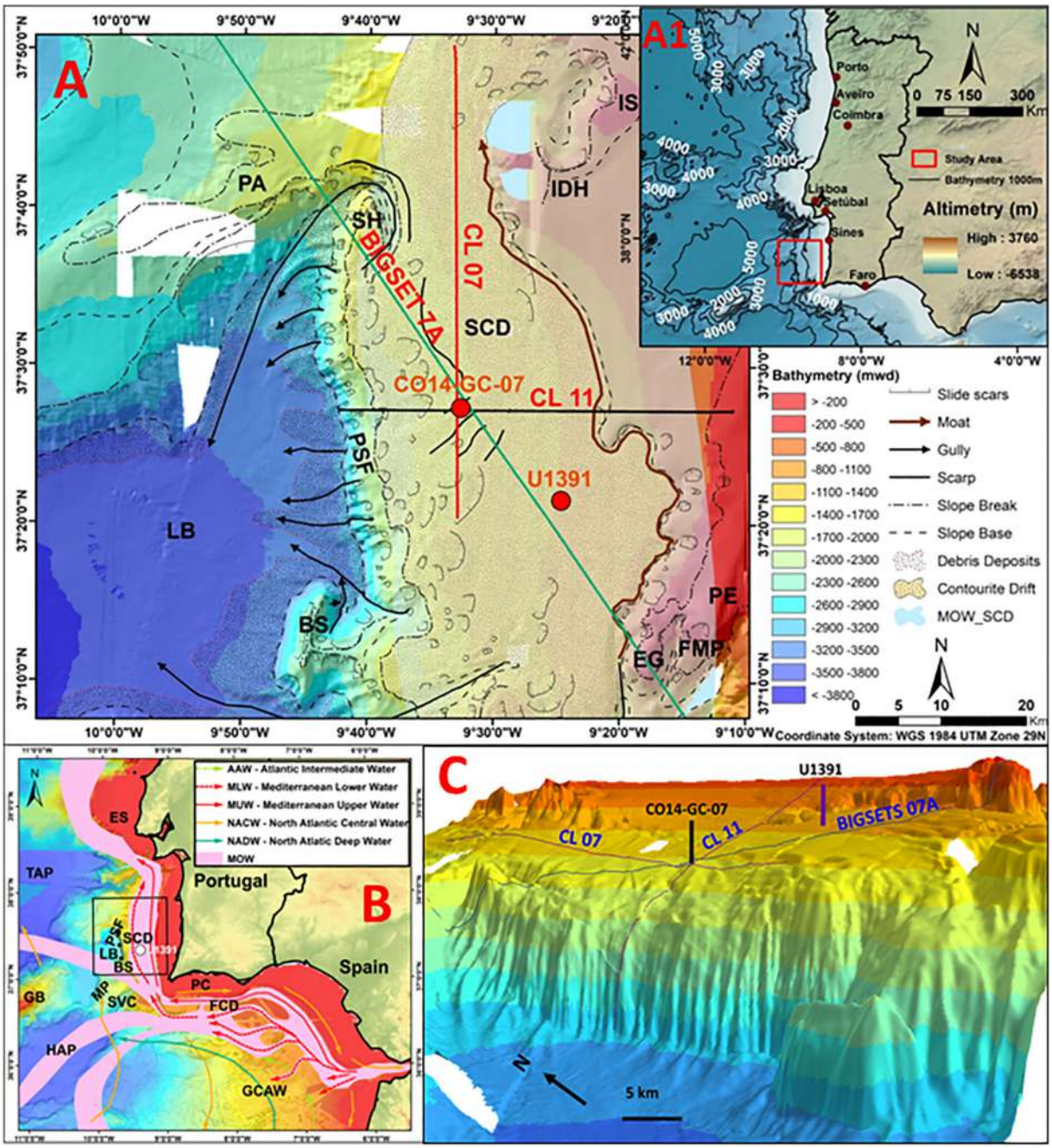

Fig. 1. Regional setting of the Alentejo Margin. (A) Geomorphologic setting. Black, red and green lines correspond to seismic lines CL 11, CL 07 and BIGSET 7A. Red dots refer to gravity core CO14GC-07 and IODP site U1391. Blank holes correspond to no data. EG – Estêvão Gomes hill; FMP – Fernão Mendes Pinto hill; IDH – Infante Dom Henrique hill; IS – Infante Santo hill; PA – Príncipes de Avis Seamounts; SH – Sines Hook. (A1) Location of the study area. Bathymetry obtained from GEBCO data (GEBCO, 2003). (B) Bottom current directions. BS – Bow Spur; ES – Estremadura Spur; FCD – Faro Contourite Drift; GB – Gorringe Bank; GCAW – Gulf of Cadiz Accretionary Wedge; HAP – Horseshoe Abyssal Plain; LB – Lebre Basin; MP – Marquês de Pombal fault; PC – Portimão Canyon; PSF – Pereira de Sousa Fault; SC – Setúbal Canyon; SCD – Sínes Contourite Drift; SVC – São Vicente Canyon; TAP – Tagus Abyssal Plain (C) 3D view of the area and the location of seismic lines and the gravity core.

3.1. High-resolution multibeam bathymetry, multichannel seismic and sub-bottom profiler datasets

Multibeam bathymetry datasets were acquired during the CONDRIBER (R/V Gago Coutinho) and MOWER (R/V Sarmiento de Gamboa) research cruises, respectively with Simrad EM12, EM1000 and EM3000 and Atlas HYDROSWEEP DS multibeam echo-sounders. These data were then compiled and integrated with published results from the EuroMargins project (Zitellini et al., 2009), for the southwest Iberia margin (Teixeira et al., 2019) (Fig. 1C), of which ~85 × 82 km of bathymetry correspond to our study area. The bathymetry was reclassified into classes of 300 m interval, from 200 to deeper than 3800 mwd.

CONDRIBER 2014 (CL11) and BIGSETS 1998 (BIGSETS 07A) seismic lines, with a total extension of 174 km, were used in this study (Fig. 1A, C), penetrating to >3000 ms (TWTT - two-way travel time) (Fig. 2B, C). CL lines were acquired with 4 G-Gun II *SERCEL* airguns at 3.5 m depth, with total volume of 610 and 910 in^3 (2000 psi). The shot interval was of 50 m and the sampling rate of 0.5 ms with a shooting frequency of 6, 7 and 10 s, using a 250-m length streamer composed

Table 1
AMS ^{14}C dates for gravity core CO14-GC-07.

Lab ID	Core depth (cm)	Dated material (plankt. foraminifera)	Conventional AMS ^{14}C (yr BP)	Error±	95.4% (2σ) Cal BP Age ranges	Calendar age Cal kyr Median probability
Beta-532879	56	*G. bulloides*	11,420	30	12,997–12,736	12,870
Beta-532878	144	*G. bulloides*	14,450	40	17,292–16,842	17,070
Beta-548290	158	*G. bulloides*	18,510	60	22,197–21,737	21,970
Beta-548291	171	*G. bulloides*	26,610	100	30,846–30,233	30,540
Beta-532880	200	*G. bulloides*; *G. inflata*	36,850	240	41,594–40,505	41,050
Beta-532881	294	*G. bulloides*	39,410	480	43,637–42,183	42,910

of 3 channels and 40 hydrophones each (Hernández-Molina et al., 2014a). The BIGSETS 1998 data were obtained through 48 channels with a 1-ms sample rate (Zitellini et al., 2001). Acquisition was done with a 4-airgun system – Sodera SSI GI-GUN - with a total volume of 150–250 in^3, 25 m of shooting interval and a 1200-m length streamer. Sub-bottom profiles were acquired with a parasound-P-35 parametric echo-sounder through a multi-ping maximum emission of 16 pings per second and a maximum resolution of 6.1 cm, with a primary frequency of 18 kHz and a secondary frequency of 4 kHz in a width of 200 m, getting a pulse length range between 0.17 and 25 ms. The detection of the bottom had a longitudinal beam resolution of 4.5° and 5° perpendicularly. Data processing was based on SEG-Y output data through filters, using the program Hotshot © (Hernández-Molina et al., 2014a). Water body salinity data used for joint analysis with seismic data was obtained from Schlitzer (2018).

3.2. Gravity core CO14-GC-07

Gravity core CO14-GC-07, with a length of 350 cm and diameter of ~8.5 cm (Fig. 3A), was retrieved during the MOWER research cruise, with a 6 m long gravity corer. After recovery, the gravity core was cut into sections of 100 cm increments, with the last one only having a length of 50 cm. The position of CO14-GC-07 coincides with the western boundary of the SCD, at ~16 km NW of IODP Site U1391, crossing the CONDRIBER CL07 and CL11 and close to BIGSETS 07A seismic lines (Fig. 1A, C).

3.3. Sedimentologic analyses

The core sections were split into two halves, with the work and archive halves being stored in the cold temperature core repository of

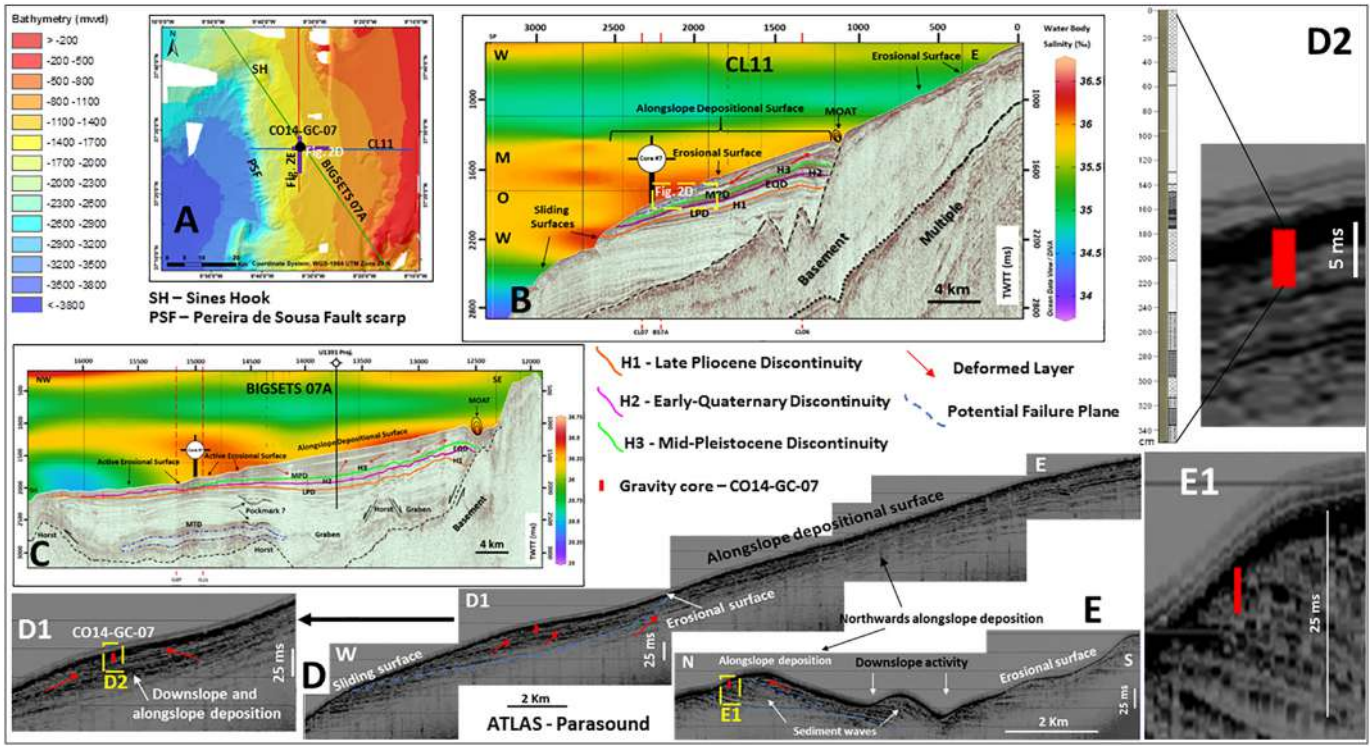

Fig. 2. Location of the CO14-GC-07 gravity core. (A) Study area with location of seismic lines and gravity core. Location of the gravity core CO14GC-07, and the Seismic Lines CL11 and BIGSETS 07A, and ATLAS Parasound lines. SH – Sines Hook; PSF – Pereira de Sousa Fault scarp. (B) Seismic Line CL11. Blue-dashed line refers to probable sliding surface. Blue-dashed line refer to stratigraphic horizon discontinuities, corresponding to internal sediment deformation; MOW – Mediterranean Outflow Water. (C) Seismic Line BS07A. Black arrows refer to active erosional surfaces. Blue-edged features and red arrows refer to stratigraphic horizon discontinuities with chaotic facies, probably indicating sediment deformation; U1391 proj. - projected IODP site U1391 - Expedition 339. (D) East-West echofacies line (Atlas Parasound). Blue-dashed lines refer to potential failure plane and red arrows refer to deformed layers; (D1) Detail of the core surrounding area; (D2) Correlation of the core CO14-GC-07 with Parasound data. Visual description of the core on the left side; (E) North-South echofacies line. Lines and arrows as in (D); (E1) detail of the core correlated with Parasound data. General - TWTT – two-way travel time; ms – milliseconds. H1 – Late-Pliocene Discontinuity (LPD, 3.2–3.0 Ma); H2 – Early Quaternary Discontinuity (EQD, 2.4–2.0 Ma); H3 – Middle Pleistocene Discontinuity (MPD, 0.9–0-7 Ma).

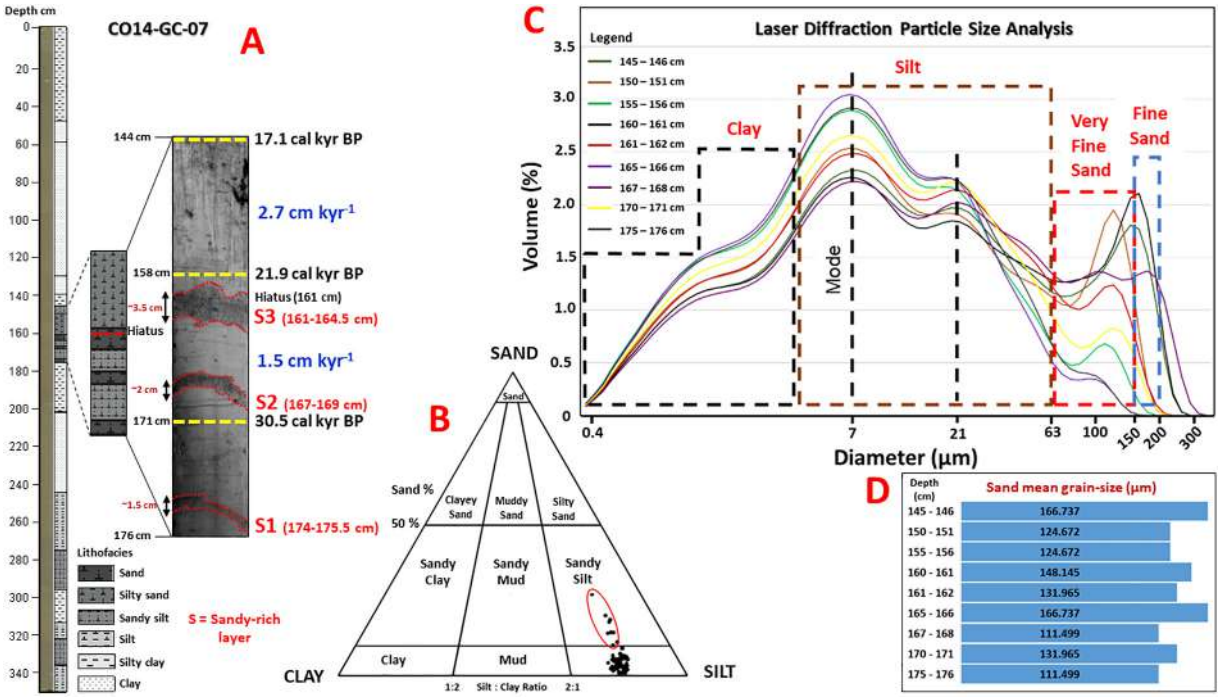

Fig. 3. CO14-GC-07 gravity core. (A) Core 7 with the visual description. A section is highlighted through a black and white image. Brightness and contrast have been adjusted. Darker units (S1, S2 and S3) correspond to sandy-rich layers. Yellow dashed-lines represent the depths of AMS ^{14}C dates and values in blue (cm kyr^{-1}) indicate sedimentation rates in the intervals between yellow dashed-lines. (B) Grain-size analysis in a sand-silt-clay trigonal diagram. Black dots refer to the core samples analysed in this work. Coarser material is highlighted by the red ellipse. (C) Grain-size curves retrieved from the laser diffraction particle size analyser. (D) Sand mean grain-size (µm) for the interval 176–144 cm, emphasized in (A).

IPMA's Marine Geology Division (DivGM). Subsamples for destructive sedimentological and environmental magnetic analyses and dating were extracted from the working halves. The non-destructive analyses (physical properties, X-ray fluorescence scanning and visual description) were performed on the archive half. Visual description allowed for the detection of bioturbation including ichnofossil traces and variations in colour.

3.3.1. Grain-size measurements

Grain-size was determined on ~10 g of bulk sediment material collected every 5 cm, for 72 samples. Samples were weighted prior and after freeze-drying to obtain the wet and dry weights, respectively. Hydrogen peroxide was used to remove organic matter from the freeze-dried samples, which were then submitted to a 60 °C warm water bath and washed with distilled water through ceramic candles to remove excess reagent. Afterwards the samples were analysed in a LS 13 320 Laser Diffraction Particle Size Analyser (COULTER ®) at the Sedimentology and Micropaleontology laboratory of the Marine Geology and GeoResources Division of the Portuguese Institute for the Sea and the Atmosphere (DivGM-IPMA). Each analysis determined grain-size spectra between 0.4 and 2000 µm. Measurements were replicated three times in order to guarantee the quality of the used dataset and the average was calculated. Precision of measurements was obtained through percentile D_{90}. Data analysis was performed using the Gradistat© program.

3.3.2. Carbonate measurements

Carbonate and organic carbon contents determination was done at 5 cm resolution following the methodology described in Abrantes et al. (1998) and Abrantes (2016), on ~1 cm^3 sediment samples taken from the same depth as the grain-size samples. Samples were dried and then grinded using a Pulverisette 7 ® rotary equipment. Then, each sample was divided into two sub-samples. One subset was directly run in a TruSpec® Micro CHNS LECO elemental analyser to measure the total carbon content (TC), as weight percent (wt%). The other subset was subjected to combustion during 8 h on predefined steps of 1 h at 200 and 300 °C and 3 h at 400 °C, to remove the total organic carbon (TOC) and analysed for inorganic carbon content (IC; wt%). This corresponds to the carbonate carbon and is referred to as $CaCO_3$ in text. The TOC was quantified by the difference between TC and IC (TOC = TC − IC). The carbonate (wt %) was calculated as the product of the inorganic carbon concentration by the factor of 8.332 (e.g., Yamamoto et al., 2000). For each level the accepted value is the mean of 3 replicates unless the first two are equal to the millesimal. The analytical precision was <1% of relative standard deviation. These analyses were also performed in the Sedimentology and Micropaleontology laboratory of the DivGM-IPMA.

3.4. Physical and geochemical properties

Volumetric magnetic susceptibility (K, 10^{-5} SI), gamma-ray density (g cm^{-3}), electrical resistivity (Ω.m) and fractional porosity (%) were determined every 1 cm on half-round core sections, through non-destructive analyses on the Geotek Multi-Sensor Core Logger (MSCL) of the University of Vigo. The abundance and distribution of Fe, Si, Ti, Ca, K were determined by X-ray fluorescence (XRF) and the respective ratios of elements were performed to assess the terrigenous or biogenic provenance of the sediments. This non-destructive analysis was carried out with an ITRAX XRF-core scanner with a Mo tube (Cox Analytical Systems) at the CACTI of the University of Vigo. Volumetric magnetic susceptibility was also measured by ITRAX, thus allowing results to be compared, and is here denoted as K_I (10^{-5} SI). The EDXRF – energy dispersive X-ray fluorescence – analysis used a step-size of 5000 µm, tension of 30 kV, intensity of 55 mA and a timestep of 20 s. EDXRF data results were obtained through CoreScanner software © (version 8.6.3), whereas data reassessment was done using Q-Spec © (version 8.6.0).

3.5. Environmental magnetic analyses

These analyses comprehend continuous measurements (i.e., at 1 cm increments) of volumetric magnetic susceptibility (K) conducted by ITRAX-XRF (K_I) and by MSCL (K_M), complemented by discrete mass-normalized measurements of several magnetic parameters conducted for a total of 106 cubic samples (8 cm^3), collected approximately every 3 cm. These analyses were used to infer the main magnetic phases, their relative concentration and granulometric state along the core length. A MFK1-FA kappabridge, spinner magnetometer JR6 (used in low velocity mode), a LDA-3A demagnetizer coupled with a PUMP magnetizer (AGICO) and an impulse magnetizer (IM-10-30; ASC Scientific) enabled the measurements of the following magnetic parameters: (i) Low-field magnetic susceptibility (mass normalized, χ_{LF}) and its frequency dependence (χ_{FD}) measured at 976 and 15,616 Hz; (ii) anhysteretic remanent magnetization (ARM) acquired under the application of 50 μT direct field and 100 μT alternating magnetic field; (iii) isothermal remanent magnetization (IRM) acquired under the application of a magnetic field of 1.0 T (considered as saturation of IRM – SIRM); and (iv) S-ratio ($SR_{300} = IRM_{300} / SIRM$) acquired through an acquisition of a backfield with 300 μT over SIRM, enabling the quantification of soft versus hard coercivity magnetic phases contribution to SIRM. These analyses were performed at Lisbon University (Laboratory of Palaeomagnetism, Instituto Dom Luiz).

3.6. Geochronology

Six planktonic foraminiferal samples of *Globigerina bulloides* (*G. bulloides*) species selected from the fraction >250 μm, and *Globorotalia inflata* for the sample at 200 cm, because of the scarcity of *G. bulloides*, were dated by accelerator mass spectrometer (AMS) ^{14}C by Beta Analytic Inc. (Beta; USA) (Table 1). The AMS ^{14}C dates were calibrated to calendar years Before Present (BP) (before present: 1950 CE) through BetaCal 3.21, using the High Probability Density Range Method (HPD), through Bayesian analysis (Bronk Ramsey, 2009) and the MARINE13 calibration data (Reimer et al., 2013) without any additional local reservoir correction.

4. Results

4.1. Morphologic and acoustic framework of the area

The SCD covers an area of ~2311 km^2, ~35 km wide and ~98 km long, within the study area (Fig. 1), with a mean slope gradient of ~5° at the seafloor surface, >1612 ms thick-TWTT, being limited eastwards by a moat that extends for ~84 km in the base of the upper continental slope, at ~800 mwd, and westwards by the Pereira de Sousa Fault scarp at ~1700 mwd (Fig. 1A).

Gravity core CO14-GC-07 was retrieved in the western limit of the SCD, near the top of the Pereira de Sousa fault scarp (Fig. 2A, B), in the transition between the middle and the lower continental slope of the Alentejo Margin and near the present-day interface of the MOW and the NADW. This core has been retrieved on a field of sediment waves (Fig. 2D, E), where some discontinuities affect their internal structure. The depositional evolution on the core site seems to change the pattern at the middle of the core, according to the reflectors of the sub-bottom profiles (Fig. 2D2, E1). This site is located in an area where intense slope instability currently occurs (Teixeira et al., 2019), and where both alongslope and downslope activity coexist (Fig. 2D, E). This is a west-dipping area, where multiple incisions occur on the top of the Pereira de Sousa fault scarp, laterally confining the core site (Fig. 2D, E), thus indicating downslope activity. This is confirmed by the presence

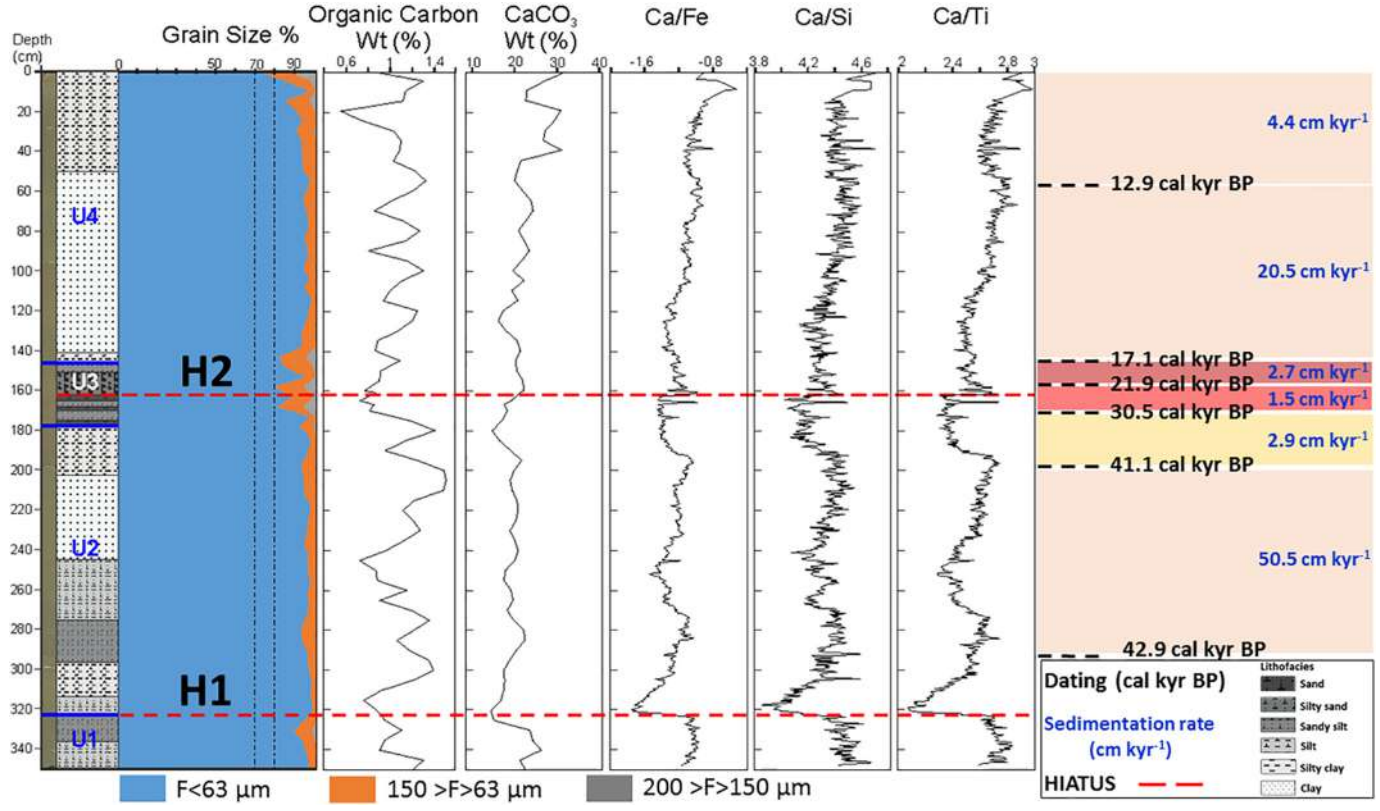

Fig. 4. Downcore plot of calcimetric properties of core CO14-GC-07. Black dashed lines in right panel indicate levels of listed calibrated AMS ^{14}C ages. Blue lines in left panel delimit the lithological units (U1-U4). Red dashed lines and H1 and H2 mark the two hiatuses identified based on sediment properties.

of 0.5- to ~11.5-km^2 landslide scars between ~1400 and ~1700 mwd (Fig. 1A), which coincides with the depth range of MOW's present-day lower limit and the interface with NADW, at ~1500 mwd (Schönfeld and Zahn, 2000). Those erosional and sliding surfaces truncate subsurface sedimentary layers (Fig. 2B, D, E). Beyond the surface instability (Figs. 1A, 2B–D), subsurface potential failure planes and chaotic seismic facies also occur below the core site (Fig. 2D, E), evidencing stratigraphic discontinuities that attest to slope instability. This mainly occurs above the Mid-Pleistocene discontinuity. The present-day seafloor, between ~800–1700 mwd, is shaped by NE-SW oriented sediment waves (Fig. 2D, E) with amplitudes ranging from 23 to 31 ms and wavelengths between 664 and ~ 3018 m. Such waves are also detected buried beneath Quaternary sediments (Fig. 2B).

4.2. Sediment properties: global performance

4.2.1. Colour and texture

Core CO14-GC-07 is mostly constituted of silty and clayey sediments with few fine and very fine sand sections (Fig. 3A). Sediment colour varies from yellowish olive (10YR 5/4) to olive grey (5Y 5/7) according to Munsell's classification, with brownish (olive brown) clayey and silty-clay layers, and greyish (olive grey) silty and sandy layers (Fig. 3A; Supplementary data).

The grain-size distribution pattern shows that 33 samples (46%) have a bimodal curve, with dominant diameter ranges of ~6.5–7.0 μm (dominant mode) and ~21 μm. About 33% have trimodal curves with peaks at ~6.5–7.0; 21 and 110–120 μm. Only 17% of the curves are unimodal with a maximum at ~7 μm. About 4% are polymodal, with more than three peaks, especially at the top of the upper ~20 cm and at the depth range of 144–176 cm (Fig. 3C), where most of the curves are trimodal and polymodal, essentially corresponding to silty, and fine and very fine sandy samples.

4.2.2. Carbonate and organic carbon

Carbonate ($CaCO_3$) and organic carbon (TOC) content are especially sensitive to grain-size variations (Fig. 4). Organic carbon content, which indicates marine/biogenic activity decreases with sediment coarsening (Fig. 4). Carbonate carbon ($CaCO_3$) shows a more regular pattern than organic carbon. There is an increasing concentration of $CaCO_3$ towards the top of the core. In coarser sediment layers $CaCO_3$ mostly increases, while TOC typically shows the opposite behaviour (Fig. 4). In general, $CaCO_3$ gradually increases upwards, reaching the maximum (3.94 wt %) near the top, at 0–1 cm, while its minimum value (1.76 wt%) occurs at 320 cm depth. The difference between $CaCO_3$ and TOC increases above ~160 cm, especially in the core's topmost 40 cm (Fig. 4).

4.2.3. Physical properties

Physical properties as magnetic susceptibility (10^{-5} SI), density and porosity, and resistivity give a clue of the origin and main composition of the sediments. The density varies between $1.58 > \rho > 1.60$ g cm^{-3} (53.5%) and mostly coincides with variations in grain-size (Fig. 5), indicating varied depositional contributions. Magnetic susceptibility has a bottom-up decreasing trend, with peaks coinciding with hiatuses in the sedimentary record (Figs. 5, 7). Resistivity (Ω·m) displays a dual behaviour as it develops close to 0 Ω·m, or even negative from the base

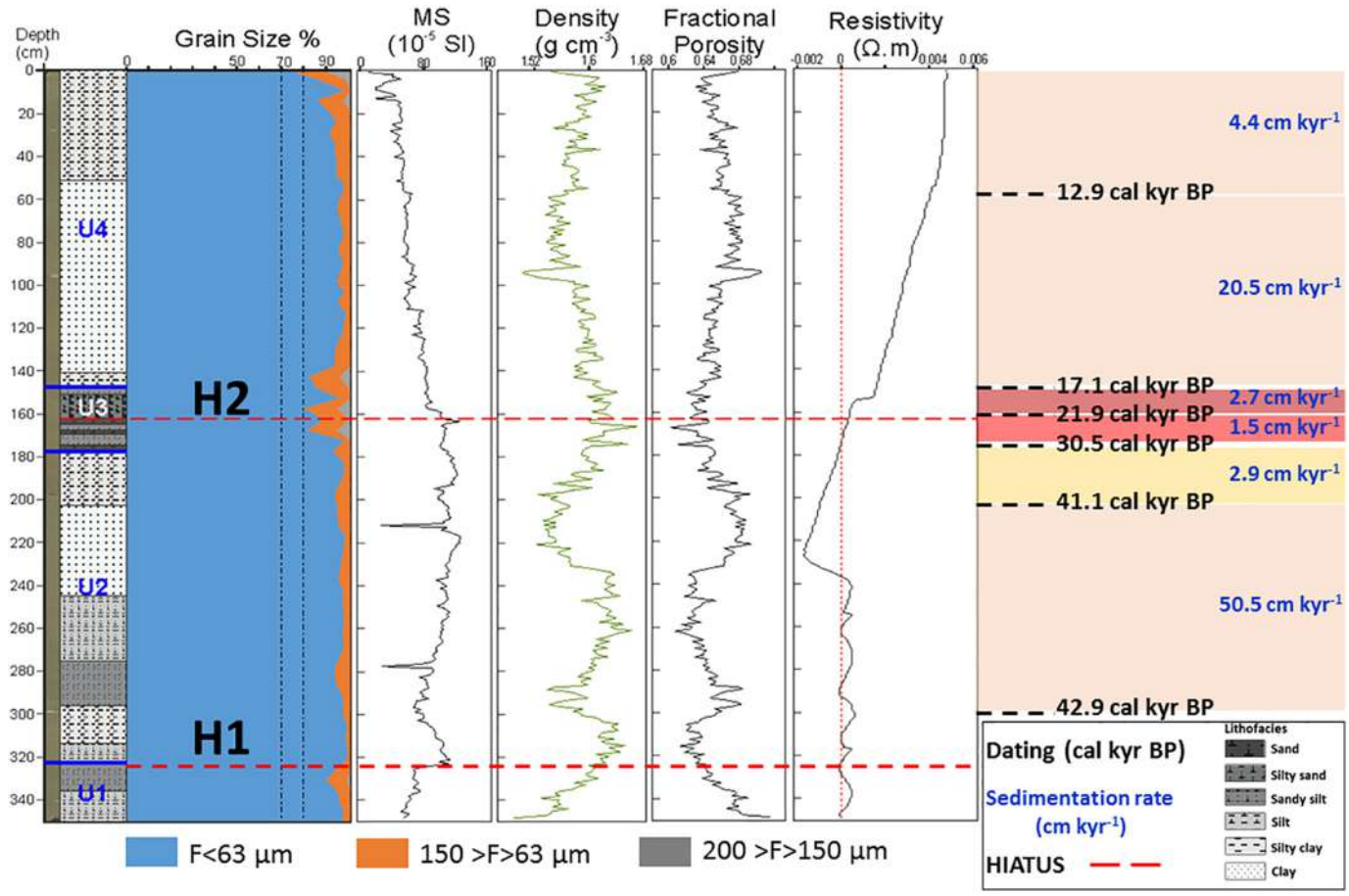

Fig. 5. Downcore plot of physical properties of core CO14-GC-07. Magnetic susceptibility (10^{-5} SI), Density (g cm^{-3}), Fractional porosity, and resistivity (Ω·m). Lines, labels and numbers as in Fig. 4.

until ~170 cm, and then it becomes positive with an increasing trend until the top (Fig. 5).

4.2.4. Geochemical properties

Geochemical properties reflect the origin of sediments, i.e., terrigenous or biogenic/marine. Terrigenous elements (Fe, K, Rb) and ratios (Fe/Ca) decrease bottom-up, whereas biogenic elements (Ca, Sr) and biogenic derived ratios (Ca/Fe; Ca/Si; Ca/Ti) tend to increase in finer sediments, being mainly concentrated above 144 cm (Fig. 6).

4.2.5. Environmental magnetic analyses

Magnetic susceptibility was measured in a continuous (volumetric K_M and K_I) and discrete (mass-normalized – χ_{LF}) ways (Figs. 5, 7). Such data are comparable, agreeing with the major features like sharp increase at ~160 cm and decrease at ~320 cm depth, general decrease from ~320 cm depth towards the top and significant variations at the uppermost 20 cm. K_I and χ_{LF} display very similar curves, which are in close agreement with Fe content (compare Figs. 6, 7). This also indicates that K_I and χ_{LF} are sensitive to Fe amount. Accordingly, henceforth we will use K_I as the reference for volumetric magnetic susceptibility. K_I and χ_{LF} show comparable results with some rare exceptions when K_I values drop suddenly at depths around 94, 194 to 294 cm, corresponding to the limits of core sections, and so, are artefacts unrelated to the magnetic characteristics of the sediment. The low values of K_I and χ_{LF} denote low amounts of ferromagnetic (s.l.) phases (e.g., Borradaile and Henry, 1997; Evans and Heller, 2003), a result commonly observed in marine sediments (Liu et al., 2012; Roberts, 2015; Silva et al., 2020). SR_{300} mostly displays stable values around 0.9 indicating that ~90% of the remanence is carried by soft coercivity magnetic minerals (as magnetite or its oxidized members), while the remaining 10% mostly result from hard coercivity components, like hematite (O'Reilly, 1984; Dunlop and Özdemir, 1997). Therefore, variations of remanence magnetic parameters along the core will be mostly sensitive to the concentration (IRM, ARM) and granulometric state (ARM/IRM) of the ferromagnetic soft phases. Together, the magnetic parameters here analysed permit the identification of two main intervals with a boundary at 161 cm depth. Within each interval, the observed variations seem to be in close agreement with lithofacies transitions (Fig. 7).

4.3. Sedimentary units

The sedimentary record CO14-GC-07 is sub-divided into four units, U1 to U4, from bottom to top, based on the analysis of qualitative and quantitative parameters. The qualitative parameters comprise colour, and sedimentary structures, unit boundaries; grain-size vertical trend and bioturbation. The quantitative ones comprise texture, $CaCO_3$ and TOC (Fig. 4), physical (Fig. 5), geochemical (Fig. 6), and environmental magnetic properties (Fig. 7).

4.3.1. Unit 1 (350–322 cm)

The top limit (322 cm) of this 28-cm thick interval is marked by an abrupt break in all properties (Fig. 4). This unit consists of light olive grey (5Y 5/7) coloured sandy mud and muddy sediments, with low to moderate bioturbation (BI = 2–3), according to the index of Taylor and Goldring (1993), with an upwards increase in organic matter and shell fragments (Figs. 4–7). In this interval, grain-size has a general bimodal behaviour, varying between 0.38 μm and 282.10 μm with a marked mode of ~6–7 μm. In this unit, ~94% of the sediments are silt and clay (F < 63 μm); ~6% correspond to very fine sand (150 > F > 63 μm); and only ~0.4% is fine sand (200 > F > 150 μm). Carbon content decreases by 1.47 wt% between the base (340 cm) and the top (322 cm) of the unit (Fig. 4). Geochemical properties present a global bottom up constancy, with both terrigenous (Fe, Rb, K) and biogenic (Ca, Sr) elements presenting a regular pattern until the top of the unit (Fig. 6).

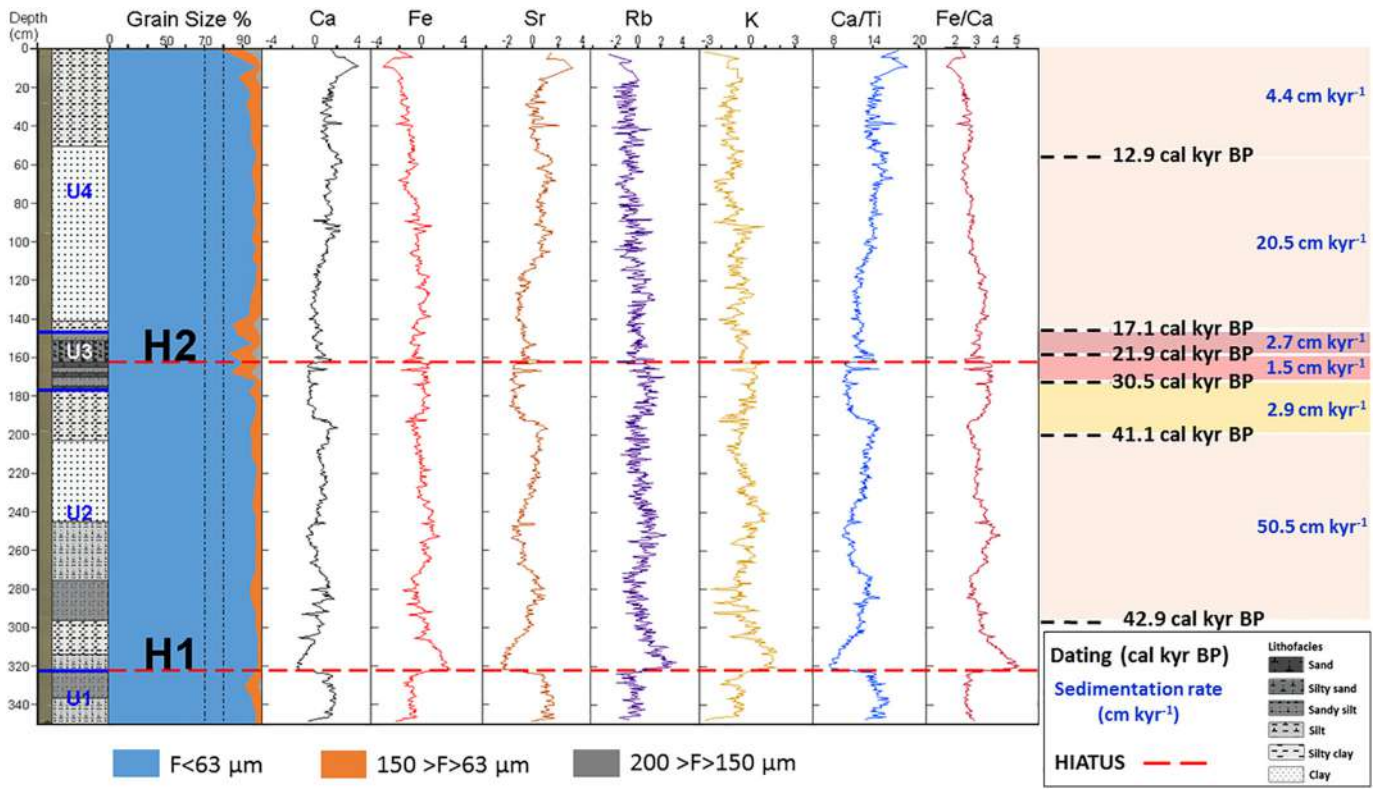

Fig. 6. Downcore plot of XRF derived geochemical properties of core CO14-GC-07. XRF derived terrigenous (Fe; Rb; and K) and biogenic (Ca; and Sr) elements (Ln), and ratios of calcium over titanium and iron over calcium are presented to support the analysis of the sedimentary input and depositional evolution along the sedimentary record. Lines, labels and numbers as in Fig. 4.

Density increases upwards from 1.49 g cm^{-3} to 1.62 g cm^{-3} between the core bottom and 320 cm depth, where an inverse trend occurs. Resistivity remains close to 0 throughout the unit (Fig. 5). For magnetic parameters, there is stability between the base and 337 cm, above which a sharp increase of SIRM and susceptibility values occurs indicating an abrupt increase of the concentration of ferromagnetic phases, with a maximum around 322 cm (Fig. 7). This increase results from the presence of ferromagnetic phases with heterogeneous magnetic granulometric states, as inferred from the increase tiny particles with superparamagnetic behaviour (increase of χ_{FD}) and increased coarser particles (decrease of ARM/SIRM). SR_{300} values show a slight but coherent decrease which could indicate a slight increase of ferromagnetic phases with higher coercivity.

4.3.2. Unit 2 (322–176 cm)

This 146-cm interval comprises thin (<3 cm) muddy layers (sandy silt, silt, silty-clay, and clay) ranging from light olive brown (5Y 5/5) to greyish brown (2.5Y 5/2), showing moderate bioturbation (BI = 3). Ichnofossil traces (*Zoophycus*) occur at ~250 cm depth, indicating biogenic activity. These sediments mostly present a massive structure with considerable organic matter and shell fragments, as well as brown oxidation traces especially in the transition from finer to coarser layers. Grain-size varies between 0.38 and 194.20 μm. With some trimodal curves, the dominant mode occurs at 7.40 μm, where 95% of the sediments are silt and clay (F < 63 μm), 4.4% are very fine sand (150 > F > 63 μm) and 0.03% are fine sand (200 > F > 150 μm). Carbon content presents a stable trend from the base to the top of the unit, although in the 195–180 and 180–160 cm range depths slight decreases (0.87 wt%) and increases (0.93 wt%) occur, respectively. The lowest $CaCO_3$ value (1.76 wt%) of the whole core occurs at 320 cm, near the unit's lower limit, coinciding with an abrupt change in all properties (Fig. 4). The evolution of biogenic and terrigenous geochemical elements shows a general decrease of 5% for Ca and 14.4% for Sr, from 322 to 176 cm (Fig. 6). Terrigenous elements present slight increases between 322 and 176 cm, of 1.5% (Fe), 1.6% (Rb) and 0.1% (K). Magnetic susceptibility, although decreasing towards the top of the unit, from ~60 (10^{-5} SI) to ~43 (10^{-5} SI), has a signature quite similar to density, whereas porosity has a pronounced negative correlation with density (Fig. 5). Density reaches its maximum (1.66 g cm^{-3}) at 259 cm and its minimum (1.52 g cm^{-3}) at 219 cm. Conversely, fractional porosity presents at those depths its minimum (61%) and its maximum (69%), respectively (Fig. 5). Resistivity values oscillate around 0, falling below this threshold between 235 cm and 176 cm.

The magnetic parameters in this interval show variations that closely follow a sinusoidal curve, with exception of χ_{FD} and S_{R300} (Fig. 7). Considering the sinusoidal curves of K_I or χ_{LF} as reference, it is verified that ARM/IRM is in phase opposition for the whole unit, while ARM and IRM are in phase opposition from 300 to 270 cm but mostly in-phase from 270 to 176 cm. This implies that grain size has an important role in IRM and ARM values. It is known that thinner ferromagnetic particles in the range of SD granulometric state have low magnetic susceptibility values and high and stables remanences while coarser grains carry inverse properties (e.g., Dunlop and Özdemir, 1997; Hrouda et al., 2006). Accordingly, the positive correlation between magnetic susceptibility values and concentration of ferromagnetic carriers is not always direct. This interpretation is reinforced by the poor correlation between IRM and χ_{LF} values. Considering such variations, as well, χ_{FD} evolution, it is possible to divide this interval in several segments, which are closely correlated with lithofacies transitions (compare grey areas with lithofacies limits at Fig. 7).

4.3.3. Unit 3 (176–144 cm)

This ~32 cm-long interval of sandy-mud and muddy layers with few shell fragments is olive (5Y 5/2) and dark grey (5YR 4/1) in colour and moderately bioturbated (BI = 3). It is distinguished from the other units by having layers of ~1.5 to ~3.5 cm thick with higher sand content (Fig. 4). About 88% of the sediments in this section correspond to fine grain-size materials – silt and clay - (F < 63 μm), whereas ~9.5% represent very fine sands (150 > F > 63 μm) and 2.3% fine sands (200 > F > 150 μm). Grain-size in this interval varies from 0.38 up to 339.90 μm, with a dominant mode of 7.30 μm (Fig. 3C), although most of the grain-size curves are trimodal (145–146; 150–151; 160–161; 161–162 cm) or even polymodal (165–166 cm). The mean grain-size of the

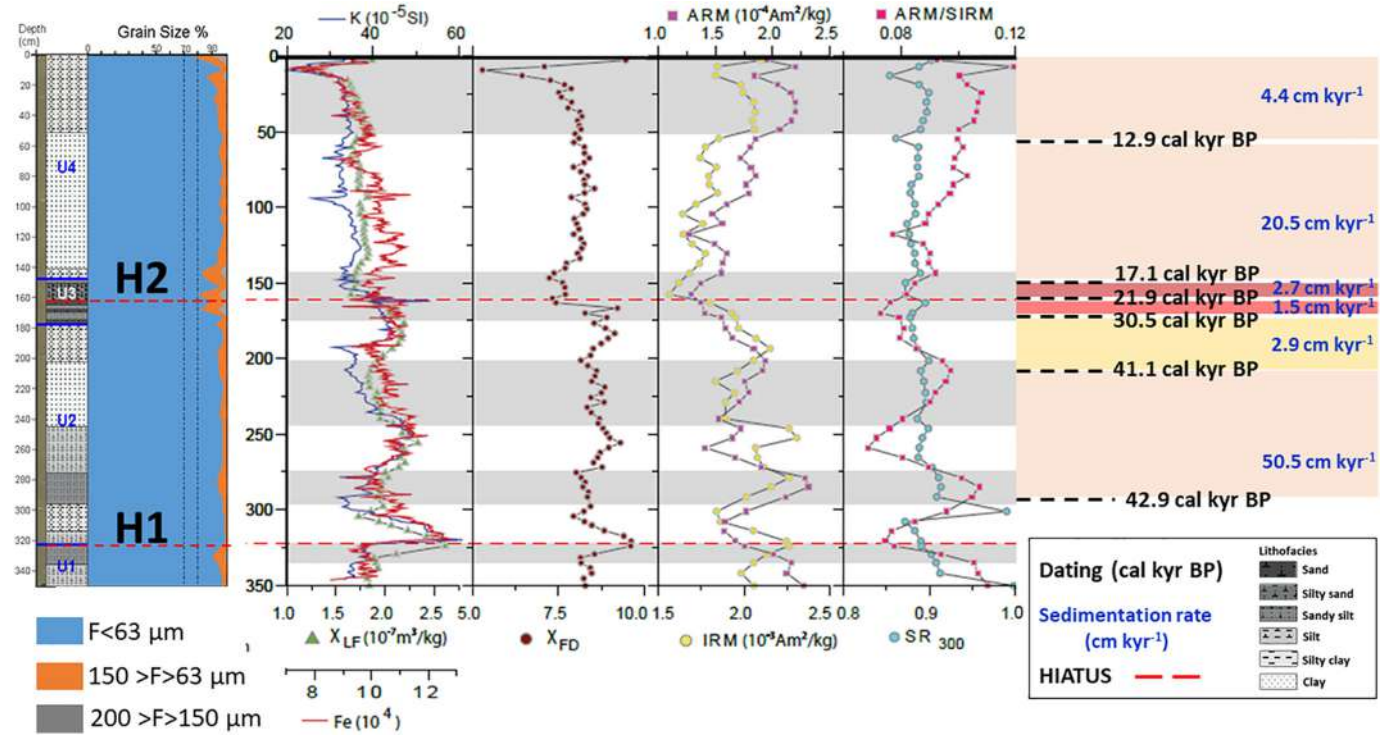

Fig. 7. Environmental magnetic analysis. Iron content (Fe). Volumetric magnetic susceptibility (K). Low-field (χLF) and frequency dependence (χFD) magnetic susceptibility. Anhysteretic remanent magnetization (ARM), Isothermal remanent magnetization (IRM). Grey bands mark magnetic peaks. Lines, labels and numbers as in Fig. 4.

sandy fraction is ~135.32 μm and the mode is ~166.73 μm. Coarser sands are present at 145 and 165 cm (~166.73 μm), whereas an intermediate sand size (~148.14 μm) occurs at 160 cm and a finer mean grain-size (111.50 μm) at 167 and 175 cm (Fig. 3D).

This interval defines a major transition at 160–161 cm depth, being common to all the remaining properties (Figs. 4–7). TOC varies from 1.10 to 0.67 wt% between 175 and 165 cm. The $CaCO_3$ content increases from the minimum of this interval (17.46 wt%) at 175 cm, to 22.76 wt% at 160 cm, decreasing again to 20.79 wt% at 145 cm (Fig. 4). There is an upwards decrease in terrigenous elements and an increase on biogenic marine elements (Fig. 6). In this unit, density reaches a maximum (1.67 g cm^{-3}), while fractional porosity records its minimum (60%), at 165 cm depth (Fig. 5), increasing then towards the top of the unit. Resistivity reveals a drastic change in its behaviour, with a great increase of 0.002 Ω·m above 153 cm (Fig. 5). K_I reaches in this unit the second greatest peak (~53 × 10^{-5} SI) of the whole sedimentary record. Above 161 cm, magnetic susceptibilities and remanence parameters (IRM and ARM) are lower than below, denoting a decrease of the ferromagnetic content. Parameters sensitive to the magnetic granulometry state (ARM/IRM and χ_{FD}) infer a coarsening of ferromagnetic carriers.

Three sand-rich layers, hereafter designated as S1, S2 and S3, with erosive contacts are present within this interval. The thickness of these layers increases from the bottom to top (Fig. 3A).

S1, at 175.5–174 cm, is a ~1.5-cm olive (5Y 5/2) fine silt layer, with irregular limits (Fig. 3A), whose grain size varies between 0.38 and 234.00 μm (mode = 7.1 μm), with ~93% of the total fraction (F < 63 μm), ~6% (150 > F > 63 μm) and ~0.3% (200 > F > 150 μm). Sand mean grain-size is 111.50 μm (Fig. 3).

S2 at 169–167 cm is a ~2-cm olive (5Y 5/2) coloured sandy mud layer with moderately irregular limits (Fig. 3A). Grain-size varies between 0.38 and 340.00 μm, with a mode of 7.10 μm, where silt and clay (F < 63 μm) correspond to ~88%, while ~9% is very fine sand (150 > F > 63 μm) and ~3% is fine sand (200 > F > 150 μm). Sand mean grain-size is ~121.70 μm. This layer has more irregular boundaries than S1.

S3 consists of a ~3.5-cm olive (5Y 5/2) coloured sandy mud layer with very irregular limits (Fig. 3A), between 164.5 and 161 cm. In this layer, 83.5% of the fraction corresponds to silt and clay (F < 63 μm), while ~13% is very fine sand (150 > F > 63 μm) and ~3.5% is fine sand (200 > F > 150 μm). Grain-size varies between 0.38 and 282.10 μm with the mode between 7.00 and 7.50 μm. Sand mean grain-size is ~148.15 μm. The ages of S2 and S3 fall between ~30.5 cal kyr BP (171 cm) and ~21.9 cal kyr BP (158 cm).

4.3.4. Unit 4 (144–0 cm)

This is a silty-clay layer with shell fragments, greyish olive (10Y 4/2) to moderate olive brown (5Y 4/4) and a mottled structure (moderate bioturbation; BI = 3). The top 50 cm consist of a yellowish brown (10YR 5/4) to moderate olive brown (5Y 4/4) clay-silt layer with low bioturbation (BI = 1). Ichnofossil traces (*Zoophycus*) are present at 42 and 25 cm depth, indicating biogenic activity. About 93% of the fraction is silt and clay (F < 63 μm), 6.2% is very fine sand (150 > F > 63 μm) whereas only 0.74% corresponds to fine sand (200 > F > 150 μm). Grain-size varies between 0.38 and 373.10 μm, with a mode of ~6.46 μm, although some trimodal curves occur at the top of the record. $CaCO_3$ generally increases from the minimum (16.48 wt%) at 125 cm to the maximum (32.81 wt%) at the top of the core (Fig. 4). Organic carbon reaches the minimum (~0.51 wt%) at 20 cm and the maximum ~1.23 wt% at 55 cm (Fig. 4). Geochemical elements show an increase of biogenic (Ca = 30%; Sr = 34%) and terrigenous elements (K = 4%; Rb = 1.8%) but a bottom up decrease of 15% of Fe. This is corroborated by the upwards increasing Ca/Ti and decreasing Fe/Ca ratios (Fig. 6). Resistivity continuously increases from 144 cm to 0 cm depth (Fig. 5), while density and porosity have a regular trend upwards. Fractional porosity has a peak (70%) at ~95 cm, whereas density reaches the lowest value (1.52 g cm^{-3}) of the whole record, at this depth. From this depth towards the top, density increases to 1.54 g cm^{-3}. Magnetic parameters show in general quite stable tendencies that are abruptly interrupted at the uppermost 20 cm. From 140 cm to 20 cm depth, K_I and χ_{LF} show a gentle decrease, which indicates a slight decrease of ferromagnetic particles as observed for the Fe content (cf., Figs. 6, 7). χ_{FD} and S_{R300} present quite stable values, indicating stable amount of particles with superparamagnetic behaviour and stable proportion between soft and hard magnetic phases. The increase of IRM, ARM and its ratio agree with an increase of smaller particles relatively to coarser ones. Above 20 cm, all the parameters, with the exception of ARM/IRM, show a well-marked decrease, with minimum values being reached for a depth around 10 cm. According to these variations, we have a decrease of the soft ferromagnetic content (decrease of K, χ_{LF}, ARM, IRM and S_{R300}) and of grains with superparamagnetic behaviour (decrease χ_{FD}). The decrease of S_{R300} also indicates an increase of the hard-ferromagnetic fraction, like hematite, relatively to the soft one.

4.4. Chronostratigraphic framework

Based on six calibrated AMS ^{14}C dates the sedimentary record of core CO14-GC-07 spans from the late Pleistocene to the Holocene and indicate significant changes in the sedimentation rates (Table 1; Fig. 8).

The oldest age of 42.9 cal kyr BP at 294 cm is near the bottom of unit 2 and places those sediments into MIS 3. In combination with the age of 41.1 cal kyr BP at 200 cm it reveals that this unit is associated with the core's highest sedimentation rate of ~50.5 cm kyr^{-1} (Table 1; Fig. 8).

Unit 3 was dated at three levels yielding ages from ~30.5 cal kyr BP at 171 cm to ~21.9 cal kyr BP at 158 cm and 17.1 cal kyr BP at 144 cm, consigning this unit mostly to MIS 2. The ages indicate lower sedimentation rates of 1.5 cm kyr^{-1} at the bottom of the unit increasing to 2.8 cm kyr^{-1} at its top (Fig. 8).

The AMS ^{14}C date at 56 cm, near the top of unit 4, corresponds to 12.9 cal kyr BP. Unit 4, therefore, coincided with the onset of the last deglaciation and with a sedimentation rate of 20.5 cm kyr^{-1} was

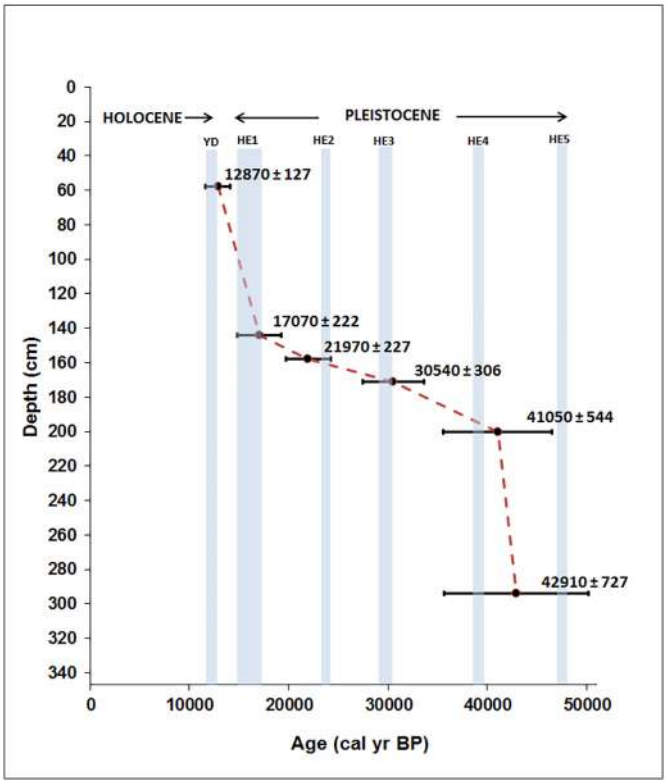

Fig. 8. Age-depth curve of the gravity core CO14-GC-07. Ages in cal yr BP with error bars (1 sigma error). The ages for Heinrich events are based on Salgueiro et al. (2014) and Stríkis et al. (2018).

again linked to higher sedimentation. In the top part of the core, encompassing mostly the Holocene, the sedimentation rate dropped to 4.4 cm kyr^{-1} (Fig. 8).

5. Discussion

The integrated analysis of the sediment properties of the gravity core CO14-GC-07 shows significant variations along the core, with grain-size being the most evident (Fig. 3). Grain-size shows a typical bi-gradational contouritic deposition, where the grain-size evolution shows a succession of coarse, fine, coarse, fine and coarse sediments from the base to the top. This evolution shows that the coarsest sediments are in the middle of the sedimentary record, between 144 and 176 cm (Fig. 3), where three sand layers appear, mainly by the action of contour currents' activity. This is attested by the remaining sediment properties (Figs. 4–7), whose signatures become highly irregular near these sandy layers where, for example, organic carbon decreases (Fig. 4) and magnetic susceptibility greatly increases (Fig. 7), demonstrating a considerable change in the depositional pattern. This contouritic deposition suggests diverse depositional phases promoted by distinct climate evolution and bottom/contour current activity.

5.1. Depositional phases: evidence from sediment properties

The analysis of the sediments' properties of core CO14-GC-07 indicate that the SCD's sedimentary evolution went through distinct sedimentary processes during four depositional phases, according to variations in grain-size and in the overall sediment properties (Figs. 4–7).

5.1.1. Phase 1 (>42.9 cal kyr BP)

This phase includes the deposition of Unit 1 (Fig. 3A). The parallel evolution of terrigenous and biogenic elements (Fig. 6) in the silty to sandy silty sediments of this phase (350–322 cm) indicates a steady depositional environment, although the occasionally coarser grain-size points to a higher energy environment caused by enhanced bottom current activity. The abrupt variations in all properties at ~322 cm mark a major change in sedimentary conditions, which is interpreted as marking an erosional hiatus (Figs. 4–7). The sharp increase of ferromagnetic concentration (IRM and χLF) around 322 cm (Fig. 7) suggests an increase in terrigenous input, generally associated with cold climatic conditions and sea-level drops (Rogerson et al., 2005; Lebreiro et al., 2009; Kaboth et al., 2017a). This interpretation is reinforced by the presence of a heterogeneous magnetic granulometric state (from small to coarser ferromagnetic particles) and increase of the hard fraction, likely due to the presence of hematite. Based on the similarity of the sediments in unit 1 and unit 2, especially the distribution of terrigenous against biogenic elements (Fig. 6), we assume that phase 1 is also of MIS 3 age.

The sharp variation in the sediment signature that occurs at ~322 cm, visible in all the sediment properties (Figs. 4–7) is interpreted as marking a hiatus (H1). The hiatus might have been caused by an erosional episode related to the stepwise sea-level drop of ~60 m between 58 and 45 cal kyr BP (Lebreiro et al., 2009), which might have influenced the vertical water mass structure and drastically changed the local sedimentary dynamics.

5.1.2. Phase 2 (>42.9–>30.5 cal kyr BP)

Phase 2 corresponding to Unit 2 (~322 and 176 cm depth), was deposited between >42.9 and >30.5 cal kyr BP, i.e. during the middle to late MIS 3. The sediment parameters reveal two main sedimentary cycles during this stage, with two peaks and two lows evident on the physical, geochemical, and magnetic properties (Figs. 5–7). In general, sediments tend to become finer upwards, spanning from sandy silt and silt to silty clay and clay, although are coarser at both limits of this phase. Between 260 and 240 cm, magnetic parameters point to a more heterogeneous magnetic granulometry, increase of the coarser (prominent low of ARM/IRM) and finer (increase of χ_{FD}) granulometry. In terms of magnetic properties, this segment shows characteristics comparable to Unit 1, despite a smaller increase of susceptibility. Extrapolating the sedimentation rate in this unit to the limits, the boundaries of phase 2 approximately coincide temporally with major sea-level drops verified during MIS 3, at 45 kyr and 30.5 kyr (Siddall et al., 2008; Lebreiro et al., 2009). The effect of these eustatic variations might be recorded in SCD sediments by an increase of biogenic and calcium related elements, during sea-level rise (Figs. 4, 6).

The calculated 1.8-kyr interval between ~42.9 cal kyr BP (294 cm) and ~41.1 cal kyr BP (200 cm) coincides with the interval from Greenland interstadial 11 to Greenland interstadial 10 (Rasmussen et al., 2014). In the SCD, this high sedimentation interval (~50.5 cm kyr^{-1}) is highly uniform. The dominantly hemipelagic sediments (Fig. 3A) suggest stable depositional conditions under the absence of significant bottom current variations at the water depth of core CO14-GC-07, possibly associated with the warmer (interstadial) conditions and their higher sea-level stands.

5.1.3. Phase 3 (>30.5–17.1 cal kyr BP)

This phase (~176 and 144 cm) spans from >30.5 to 17.1 cal kyr BP (mostly MIS 2) and corresponds to the coarsest sedimentation regime (Fig. 3). Great variability exists both in grain-size and sediment physical and geochemical properties (Figs. 5, 6). This interval marks the major transition in the behaviour evidenced by magnetic parameters (Fig. 7), where for example, above 161 cm, χ_{FL} and χ_{FD} values are on average lower than below, ARM/IRM stops with a sinusoidal pattern to present an overall increase towards the top, which is roughly followed by IRM and ARM.

Three coarser layers (S1–S3) show an increase in terrigenous concentrations with the thickest level (S3 at ~161 cm) revealing the largest variations in sediment properties (Figs. 4–7). The higher Fe/Ca and Si/Ca values (Fig. 6) in the coarser sediment layers point to higher terrigenous contributions derived from continental fluxes, mainly during low-stand sea level stages (Baas et al., 1997; Govin et al., 2012). Coarsening of magnetic phases is also inferred by the decrease of ARM/IRM values (Fig. 7). Moreover, irregularity of S_{R300} and sharp variations on the magnetic susceptibility in close agreement with Fe concentration peaks, indicate small-scale variations of concentration and type of magnetic carriers (Fig. 7).

The decrease of biogenic elements (Ca and Sr) and the increase of terrigenous elements in layers S1–S3 (Fig. 6), indicate that these layers were deposited under different processes than the remaining core. The drop in organic carbon content, which commonly occurs during colder periods (Ohkouchi et al., 2002), points to low biogenic/marine contribution due to the influence of colder (arctic) conditions, which according to Magill et al. (2018) promotes a TOC decrease.

Coarse sediment fractions and detrital sediment input can be associated with the increase of bottom current activity (Baas et al., 1997; Kaboth et al., 2017a). It is possible that the low sedimentation rates reflect sediment scarcity promoted by the MOW's high winnowing activity during MIS 2 (Schönfeld and Zahn, 2000). The sudden and large variation in all properties at ~161 cm (Figs. 4–7) indicates the existence of a second erosional hiatus (H2).

5.1.4. Phase 4 (17.1 cal kyr BP– Present)

This phase corresponds to interval 4, where high percentages (~80 to 90%) of fine sediment (<63 μm) (Figs. 4–7), indicate the dominant deposition of clay and silty clay, due to less winnowing activity, as also verified by Unit d2 of core MD9923-36 from the Faro-Albufeira drift (Llave et al., 2006). However, like in the top unit of that piston core, there is some sediment coarsening near the top of our record (Fig. 3). A higher uniformity of sediment signatures is corroborated by magnetic susceptibility and its frequency dependency, whose values are consistently stable and lower above 160 cm (Fig. 7). ARM and IRM, show some oscillations but with an amplitude lower than observed below 160 cm. The general increase of ARM/IRM towards the top indicates a gradual increase of small grains, which could be interpreted as a

diagenetic overprint. During this process small iron-oxides can experience complete dissolution, while the largest grains present an effective decrease (e.g., Rey et al., 2000, 2005; Liu et al., 2012; Roberts, 2015; Duan et al., 2017). Therefore, this process also explains the higher values of ARM and IRM observed towards the top. This evidence points to uniform sedimentation without significant perturbations. Furthermore, the increase in biogenic components when compared with depths below 160 cm, suggest a higher marine contribution. These indicate continuous and a more constant, less disturbed, depositional environment.

Between 144 cm (~17.1 cal kyr BP) and 56 cm (~12.9 cal kyr BP) there is a ~4.3 cal kyr-period, with a sedimentation rate of ~20.5 cm kyr^{-1} (Fig. 3). This period comprises the Bølling-Allerød (B-A) interstadial (warming event), which occurred between ~14.6 and 12.7 cal kyr BP (Naughton et al., 2016) and corresponds to a rising sea level (Deschamps et al., 2012) likely to favour calmer and vertical settling conditions as well as the decrease in MOW's velocity and strength, suggested for the B-A interstadial by Voelker et al. (2006) and Sánchez Goñi et al. (2016).

Above 56 cm depth (~12.9 cal kyr BP) close to the onset of the Younger Dryas, silty clay is dominant (Fig. 4). From this depth up to 0 cm, through the Holocene sedimentary succession, the sedimentation rate of ~4.4 cm kyr^{-1} probably took place in a steady depositional environment as no variations are identified in sediment properties. Moreover, there is an increasing trend in biogenic elements, associated with abundant bioturbation represented for instance by *Zoophycus*. However, there is a strong variation in all magnetic parameters around the 10 cm depth. Such variations point to a significant decrease in iron-oxides and/or increase of the hard fraction relative to the soft one, suggesting an increase of terrigenous input.

5.2. Origin of coarse layers (S1, S2, S3)

The three coarse sediment layers S1, S2, and S3, occurring between 175 cm and 161 cm represent major variations in the glacial depositional environment (Fig. 3A), as they present coarser and heterogeneous sediments with very irregular contacts. Three hypotheses regarding their origin can be proposed:

(i) IRD. The higher number of sand-sized grains could result from ice-rafted debris (IRD) deposited during Heinrich Events. IRD deposition has been recognized in the Portuguese margin by several authors (e.g., Schönfeld et al., 1993; Lebreiro et al., 1996; Baas et al., 1997; Zahn et al., 1997; de Abreu et al., 2003; Eynaud et al., 2009). Baas et al. (1997) found that the ages of the IRD-rich layers match with the ages of Heinrich Events in the central North Atlantic. It is worth to note that Zahn et al. (1997) identified three discrete IRD layers corresponding to Heinrich Events 1, 2 and 4 (Fig. 9C) in their core SO75-26KL, retrieved from 1099 mwd, ~41 km NNE from CO14-GC-07 (Fig. 9A). Those three layers are thicker (~14–18 cm thick) than the three coarser ones found in our record, which only account for ~1.5 to 3.5 cm thickness (Fig. 3A). Mean sand grain-size in S1–S3 layers varies between 111.50 μm and ~148.15 μm (Fig. 3D), so that we cannot fully exclude IRD. However, only the timing of S2 is close enough in age to potentially correspond with a Heinrich Event, namely Heinrich Event 3 for which Zahn et al. (1997) did not observe IRD deposition at the Alentejo margin.

(ii) Turbidites. Three different slope instability events could have occurred upslope (<1425 mwd) and the displaced sediments reached the area as turbidites, creating the S1–S3 thin-layered coarser levels. Some authors (e.g., Baas et al., 1997; Rasmussen et al., 2003; Lebreiro et al., 2009; Ducassou et al., 2016), recognized that downslope mass transport processes were frequent along the Portuguese margin during glacial periods led by substantial sea-level changes. Considering the mostly MIS 2 age constraints of the S1–S3 coarser layers, they likely formed during a period of relative low sea-level. Such a period can be characterized by an increasing contribution of terrigenous input (Siddall et al., 2008), favouring sediment coarsening as well as an increasing Fe content and magnetic susceptibility (Figs. 3, 6, 7). The alternation between coarse layers (S1–S3) and finer sediments indicate a change in depositional conditions and the presence of hiatus H2, in the S1–S3 layers interval could also be related to erosion due to sediment instability, which would reinforce the argument of gravitational deposition of these sediments. However, the absence of a fining-upward structure of these layers as indicated by Shanmugam (2016), and the thickening of the S1–S3 layers towards the hiatus point to an increase in contour current strength and winnowing activity rather than turbidite deposition.

(iii) Intensification of bottom/contour currents (especially MOW) activity, during colder periods. Grain-size variability is a proxy for MOW flow speed and intensity, which are higher during cooler periods (e.g., Rogerson et al., 2005; Toucanne et al., 2007; Voelker et al., 2006). During cold periods, the enhancement of MOW promoted by the increased salinity and density gradients in the interface with neighbouring bottom currents (Voelker et al., 2006; Rogerson et al., 2012) had great impact in the SCD surface, between ~1000 and 1500 mwd (Schönfeld and Zahn, 2000; Rogerson et al., 2005; Llave et al., 2006).

The increasingly coarser grain-size of S1–S3 layers and the increasingly irregular geometry of their boundaries (Fig. 3A), imply that they may be the result of high-energy events, such as bottom currents enhancement. The S1–S3 layers occurred prior to the LGM, with S3 presenting the coarsest mean sand size (~148.15 μm) and the most irregular limits (Fig. 3A, D). S3 is also the thickest and the youngest layer (Fig. 3A), thus being the closest one to the LGM. This evidence points to the action of bottom current activity through the cooling transition to the LGM. Above S3, sediments are still coarse, although do not have the configuration of the S1–S3 layers, consistent with a lower influence of MOW, which according to Schönfeld and Zahn (2000) during the LGM imprinted the continental slope of SW Portuguese margin between ~1600 and 2200 mwd, below our sedimentary record.

Considering the possible explanations previously addressed for the origin of the coarser layers S1–S3, the most plausible process is likely to be the enhanced bottom current activity that winnowed fine particles and sorted previously existing sandy sediments, in agreement with the contourite model (Faugères et al., 1984).

5.3. MOW variability during the last ~50 kyr: palaeoceanographic implications

The multiproxy analysis of the sedimentary record of core CO14-GC-07 allows for inference of the variability and vertical migration of the MOW for the last ~50 kyr, based on current knowledge about the behaviour of this water mass. Currently, MOW circulates at <10 cm s^{-1} along the western Portuguese margin (Ambar et al., 2002), although its intensity was stronger in the past, especially during Late Pleistocene glacial periods (Schönfeld and Zahn, 2000; Rogerson et al., 2005; Voelker et al., 2006; Toucanne et al., 2007; Bahr et al., 2014).

The advection of MOW left distinctive imprints along the SW Portuguese margin (Hernández-Molina et al., 2014b) during glacial and interglacial bottom current oscillations. There are signs for intensification of MOW's advection (Rogerson et al., 2005) through grain-size coarsening and increasingly irregular layer boundaries, and vertical shifting of its path (e.g., Schönfeld and Zahn, 2000; Llave et al., 2006; Kaboth et al., 2017a). Rogerson et al. (2005) found correlation between grain-size and MOW flow strength, during glacial periods, indicating that the sediment fraction coarsening reflects variations in MOW intensity (Schönfeld and Zahn, 2000; Llave et al., 2006).

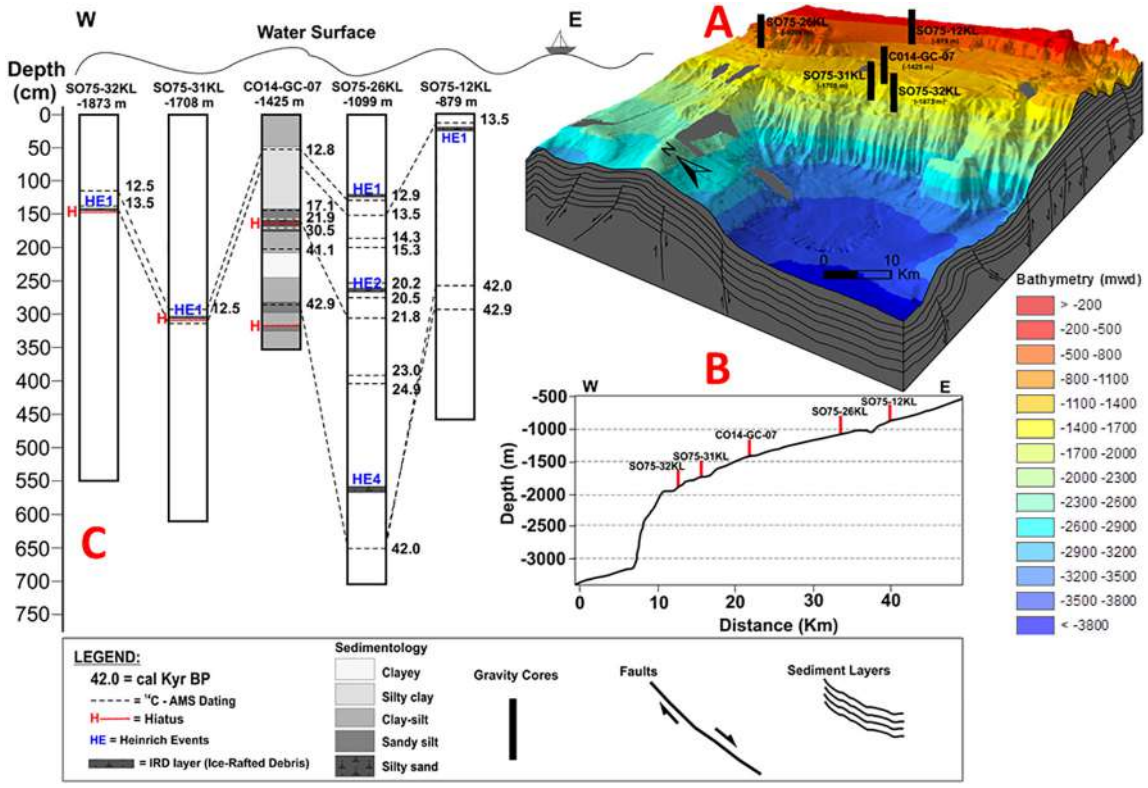

Fig. 9. Chronostratigraphic correlation between sedimentary cores retrieved from the Sines Contourite Drift. (A) 3D diagram block, with bathymetry acquired in CONDRIBER, MOWER, and SWIM projects. Black bars correspond to cores retrieved in the area: CO14-GC-07 analysed in this work and four cores previously retrieved for other works. (B) Longitudinal profile representing bathymetric position of each core. (C) Chronostratigraphic core correlation based on AMS ^{14}C dates. Dated ages, stratigraphic hiatuses (H) and Heinrich events (HE) are marked along the cores. Data of cores SO75-12-, 26, 31, and 32KL retrieved from Baas et al. (1997), Zahn et al. (1997) and Schönfeld and Zahn (2000).

As outlined above, we interpret the S1–S3 coarse layers (Fig. 3A) as being related to MOW intensification, conforming with evidence in the Gulf of Cadiz for an enhanced MOW during this period (e.g., Rogerson et al., 2005; Llave et al., 2006; Voelker et al., 2006).

The multiproxy analysis of sediment properties (Figs. 4–7) testifies to several changes in depositional conditions that can be interpreted as an indicator of MOW strength and vertical variability. Therefore, we propose four main phases of MOW's vertical oscillations during the last ~50 kyr.

5.3.1. Phase I (>42.9–~30.5 kyr cal BP)

This phase occurred during MIS 3 and is characterized by hemipelagic sedimentation in a fairly uniform depositional environment, most likely below the MOW. The presence of the S1 coarse layer (Fig. 3A), immediately before 30.5 cal kyr BP, suggests deepening of the MOW (Fig. 10A), potentially related to oceanographic changes around Heinrich Event 3 and the progressing sea level regression. A downslope shift of the upper MOW during late MIS 3 is observed by Kaboth et al. (2016) at the Faro drift.

5.3.2. Phase II (30.5–21.9 cal kyr BP)

This phase spans from the end of MIS 3 into the LGM. The two coarse layers (S2 and S3) increase in thickness, together with mean grain size and irregularity of the boundaries towards the top (Fig. 3A), indicating enhancement of MOW towards the LGM (~23–19 cal kyr BP). During this phase the SW Portuguese margin faced an intensification and deeper settling of the MOW in the water column (Schönfeld and Zahn, 2000; Rogerson et al., 2005; Llave et al., 2006; Voelker et al., 2006; Bahr et al., 2014; Kaboth et al., 2017a), exerting impact on the seafloor at deeper depths (~1600–2200 mwd). Therefore, we suggest that the coarse layers S2 and S3 testify to two episodes of MOW enhancement, which reworked and sorted middle slope sediments, when this water mass was sinking towards its deepest position (~1600–2200 mwd) reached in the LGM (Fig. 10). Furthermore, the presence of a hiatus in the sedimentary record (H2 – Figs. 3–7) at ~161 cm, closer to the LGM also suggests a stronger MOW and consequent high erosional activity, in agreement with the findings of Schönfeld and Zahn (2000) (Fig. 9C). Their cores are ~300–400 m deeper than CO14-GC-07, which suggests that in this period MOW was stronger and shifting downwards. In our record the H2 (Figs. 4–7) marks the end of the visible effects of MOW on the sedimentary record, during this time interval.

5.3.3. Phase III (21.9–17.1 cal kyr BP)

The sedimentary record corresponding to this phase is homogeneous and composed of sandy silt (Fig. 3A), suggesting strong bottom current activity, despite the depositional homogeneity and the absence of irregular contacts between sediment layers. This points to the absence of direct MOW activity at this site from the late LGM until the onset of the last deglaciation (Fig. 10A). Considering glacial MOW activity between 1600 and 2200 mwd until 14 cal kyr BP (Schönfeld and Zahn, 2000), we infer that our core (1425 mwd) was not under the influence of the MOW, but instead was likely affected by the overlying ENACW (Fig. 10A-III).

5.3.4. Phase IV (17.1 cal kyr BP–present)

Close to 17.1 cal kyr BP, the effects of the MOW were still absent on the middle continental slope (Fig. 10A–IVa), as hemipelagic sedimentation is dominant (Fig. 3A). However, after the LGM, MOW moved upslope again, reaching its present-day circulation pattern and depth at 7.5–6.0 kyr BP (e.g., Schönfeld and Zahn, 2000). Gradual sediment

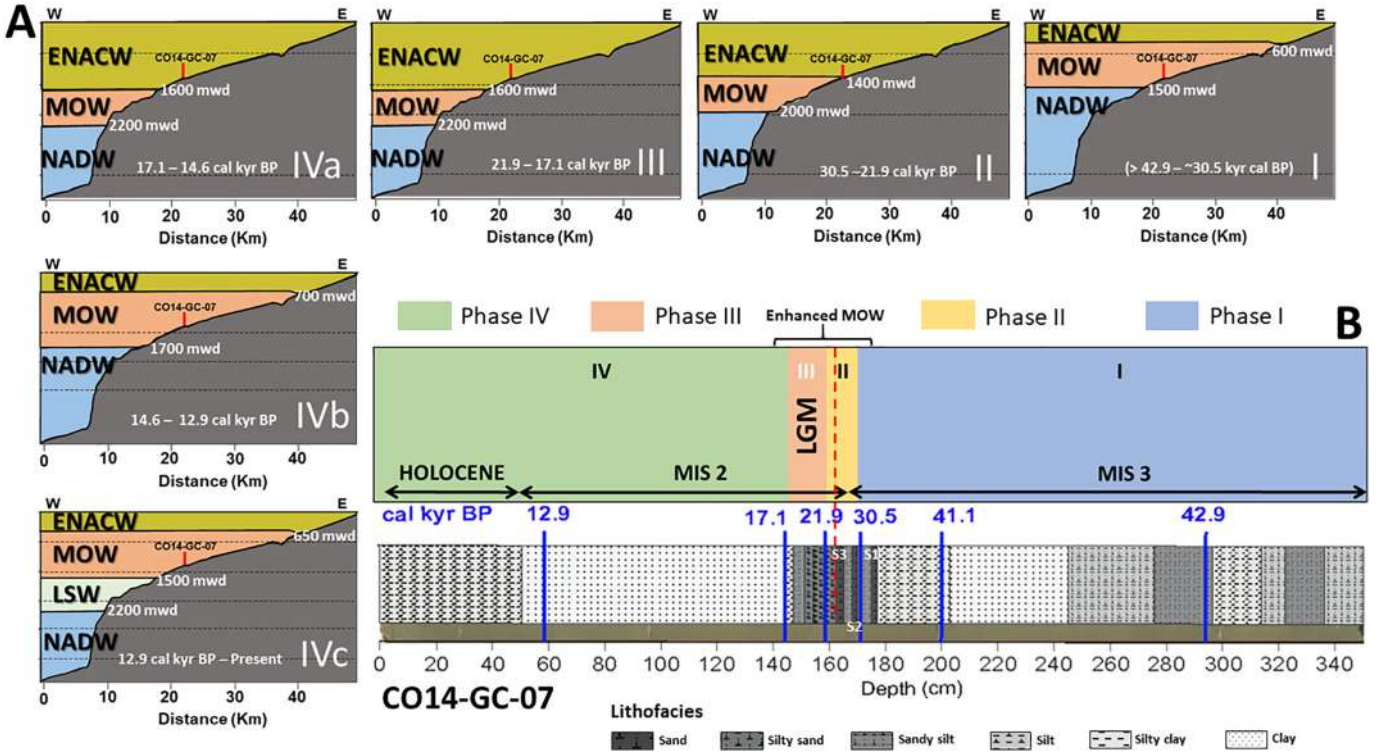

Fig. 10. Simplified evolution model of the phases of MOW during the Late Pleistocene and Holocene, in the Sines Contourite Drift. (A) MOW vertical shifting on the water column. I to IVc represent the phases of MOW. The depths in meters water depth (mwd) represent the depth of the interfaces between MOW and ENACW, NADW, and LSW (Labrador Sea Water). (B) The evolution of the sedimentary record (CO14-GC-07) through MOW phases during the Late Pleistocene and Holocene. S1–S3 are sand layers.

coarsening, from clay to silty clay, after ~12.9 cal kyr BP towards the core top (Figs. 3–7) is interpreted as reflecting an upward shift of the MOW/ENACW interface, towards its present-day position. This upward shift promoted more impact on the middle slope than in the LGM, when it was absent.

5.4. Morphosedimentary evolution in the Sines Contourite Drift related with MOW circulation

The depth of the interface between the upper and lower MOW branches roughly shifted from its glacial position at 2200 mwd to its present-day position at 1100 mwd, coinciding with the main cluster of landslide scars in the Alentejo margin (Fig. 1A, C). Most of the slide scars present at the SCD range in depth between 1100 and 2500 mwd, which partially coincides with the main cluster of sediment waves, between ~800 and ~ 1700 mwd (Teixeira et al., 2019). Both landslides and sediment waves roughly match with the depth range (1100–2200 mwd) of the vertical shifting of MOW between glacial and interglacial periods (Fig. 10). This vertical movement of MOW and its interface with NADW and ENACW may have had a key role in creating this cluster of landslides and contributed to form sediment wave fields (Fig. 2E), whereby the dynamical mixing at the respective interface results in higher current velocity and instabilities at the sea floor and decelerated current velocity in the centre of the interval to more homogenous deposition (e.g., Miramontes et al., 2019).

Water-mass interfaces constitute important pycnoclines generated by salinity and temperature contrasts, which are generally affected by baroclinic activity (e.g., McCave, 2001; Pomar et al., 2012), responsible for flow acceleration (e.g., Rebesco et al., 2014; Ercilla et al., 2016). Under these conditions, water-masses interfaces could be responsible for higher slope instability in that depth range, through the impact on the slope surface caused by enhanced water flow. Moreover, the presence of sediment waves favours the development of small slide scars through the development of surface discontinuities, as verified by Lee et al. (2002) on the margin of northern California. These discontinuities are highly conditioned by the vertical shift of local water-mass interfaces, as also verified in the Ewing Terrace (Hernández-Molina et al., 2009) and in La Plata Terrace (Preu et al., 2013) on the Argentine margin.

6. Conclusions

The multiproxy analysis of the gravity core CO14-GC-07 through sedimentological, physical, geochemical, and environmental magnetic properties, complemented by AMS ^{14}C dating, has shown that the sedimentary evolution of the SCD went through four distinct phases between >43 cal kyr BP and present. The combined variation of these properties demonstrates that these phases have different and irregular sedimentary conditions, which are mainly dependent on variable climate conditions and bottom/contour current speed variations and vertical oscillations.

The variability of the MOW represents major variations in depositional conditions, which are represented in our sedimentary record by three coarse-grained layers and interpreted as related to MOW enhancement. As bottom current enhancement is favoured by cold climatic episodes and S1–S3 layers become thicker and present a coarser mean grain-size closer to H2, we conclude that climatic cooling in conjunction with sea-level regression and increased terrigenous input caused the formation of those layers.

The vertical shifting of MOW and its interfaces with both ENACW and NADW, constitute important foci of flow acceleration and thus of greater impact on the seafloor/slope surface. This dynamic contributes for the creation of sediment waves but also for slope instability in the sedimentary stacking, leading to the development of landslide scars.

The multiproxy analysis of core CO14-GC-07 provides an extended overview of the depositional environment on the SCD during the last >43 kyr. The analysis of multiple sediment properties shows an

integrated evolution of both terrigenous- and biogenic-induced properties and glacial vs interglacial climatic events. This analysis can be effective on other continental margins with contouritic activity.

Further work must be done to understand how the constraints provoked by climate variation and bottom current activity on the sedimentary record can impact slope stability and the mechanical behaviour of those sediments.

Supplementary data to this article can be found online at https://doi.org/10.1016/j.sedgeo.2020.105737.

Declaration of competing interest

The authors declare that they have no competing financial interests or personal relationships that could have appeared to influence the work reported in this paper.

Acknowledgements

M. Teixeira thanks FCT (Fundação para a Ciência e a Tecnologia) - the Portuguese Foundation for Science and Technology – for funding this PhD (SFRH/BD/110674/2015).

The Editor, Professor Jasper Knight and an anonymous reviewer are gratefully acknowledged for their constructive comments and suggestions, which helped to improve this paper. CONDRIBER (FCT-PTDC/GEO/4430/2012) and MOWER (CTM2012-39599-C03-02) projects are acknowledged for providing the data for this work. Professor J. Hernández-Molina is thanked for enlightening discussions in an early stage of this manuscript. The authors also acknowledge the R/V Sarmiento de Gamboa and NRP/Gago Coutinho Captains and crews for their assistance during MOWER and CONDRIBER cruises, respectively. F. Abrantes, A. Voelker, E. Salgueiro, and F. Naughton thank the support of the Portuguese national funds from FCT - Foundation for Science and Technology through project UIDB/04326/2020 (CCMAR). Landmark Graphic Corporation is thanked due to Landmark University Grant Program. ESRI is thanked for the student license of ArcMap©. This publication is supported by FCT funded projects - UIDB/GEO/50019/2020 – IDL and MAGICLAND (PTDC/CTA-GEO/30381/2017), and by the FAUCES project (CTM2015-65461-C2-1-R). C. Monteiro, W. Soares, M. Freitas and A. Rebotim from IPMA are thanked for the laboratory support.

References

Abrantes, F., 2016. Data report: calcium carbonate and total organic carbon records from IODP Expedition 339 Sites U1385 and U1391. In: Stow, D., Hernández-Molina, F.J., Alvarez-Zarikian, C., Scientists, E. (Eds.), Proceedings of the Integrated Ocean Drilling Program, 339: Tokyo. Integrated Ocean Drilling Program Management International, Inc.. https://doi.org/10.2204/iodp.proc.339.201.2016.

Abrantes, F., Baas, J., Haflidason, H., Rasmussen, T., Klitgaard, D., Loncaric, N., Gaspar, L., 1998. Sediment fluxes along the northeastern European Margin: inferring hydrological changes between 20 and 8 kyr. Marine Geology 152, 7–23.

Alonso, B., Ercilla, G., Casas, D., Stow, D., Rodríguez-Tovar, F., Dorador, J., Hernández-Molina, J., 2016. Contourite vs gravity-flow deposits of the Pleistocene Faro Drift (Gulf of Cadiz): sedimentological and mineralogical approaches. Marine Geology 377, 77–94.

Ambar, I., Howe, M.R., 1979. Observations of the Mediterranean outflow-II. The deep circulation in the vicinity of the Gulf of Cadiz. Deep-Sea Research 26, 555–568.

Ambar, I., Serra, N., Brogueira, M.J., Cabeçadas, G., Abrantes, F., Freitas, P., Gonçalves, C., Gonzalez, N., 2002. Physical, chemical and sedimentological aspects of the Mediterranean Outflow off Iberia. Deep-Sea Research 49, 4163–4177.

Baas, J., Mienert, J., Abrantes, F., Prins, M., 1997. Late Quaternary sedimentation on the Portuguese continental margin: climate-related processes and products. Palaeogeography, Palaeoclimatology, Palaeoecology 130, 1–23.

Bahr, A., Jimenez-Espejo, F., Kolasinac, N., Grunert, P., Hernández-Molina, F.J., Röhl, U., Voelker, A., Escutia, C., Stow, D., Hodell, D., Alvarez-Zarikian, C., 2014. Deciphering bottom current velocity and paleoclimate signals from contourite deposits in the Gulf of Cádiz during the last 140 kyr: an inorganic geochemical approach. Geochemistry Geophysics Geosystems 15. https://doi.org/10.1002/2014GC005356.

Bahr, A., Kaboth, S., Jiménez-Espejo, F.J., Sierro, F.J., Voelker, A.H.L., Lourens, L., Röhl, U., Reichart, G.J., Escutia, C., Hernández-Molina, F.J., Pross, J., Friedrich, O., 2015. Persistent monsoonal forcing of Mediterranean Outflow Water dynamics during the late Pleistocene. Geology 43, 951–954.

Boillot, G., Girardeau, J., Kornprobst, J., 1989. Rifting of the West Galicia continental margin: a review. Bulletin de la Société Géologique de France 8, 393–400.

Borradaile, G., Henry, B., 1997. Tectonic applications of magnetic susceptibility and anisotropy. Earth Science Reviews 42, 49–93.

Bronk Ramsey, C., 2009. Bayesian analysis of radiocarbon dates. Radiocarbon 51, 337–360.

Cacho, I., Grimalt, J., Sierro, F.J., Shackleton, N., Canals, M., 2000. Evidence for enhanced Mediterranean thermohaline circulation during rapid climatic coolings. Earth and Planetary Science Letters 183, 417–429.

Caralp, M., 1988. Late Glacial to Recent Deep-Sea benthic foraminifera from the Northeastern Atlantic Cadiz Gulf and Western Mediterranean Alboran Sea. Paleoceanographic results. Marine Micropaleontology 13, 265–289.

Cherubin, L., Carton, X., Paillet, J., Morel, Y., Serpatte, A., 2000. Instability of the Mediterranean Water undercurrents southwest of Portugal: effects of baroclinicity and topography. Oceanological Acta 23, 551–573.

de Abreu, L., Shackleton, N.J., Schönfeld, J., Hall, M., Chapman, M., 2003. Millennial-scale oceanic climate variability off the W Iberian margin during the last two glacial periods. Marine Geology 196, 1–20.

Deschamps, P., Durand, N., Bard, E., Hamelin, B., Camoin, G., Thomas, A.L., Henderson, G.M., Okuno, J.i., Yokoyama, Y., 2012. Ice-sheet collapse and sea-level rise at the Bolling warming 14,600 years ago. Nature 483, 559–564.

Duan, Z., Liu, Q., Gai, C., Zhao, X., 2017. Magnetostratigraphic and environmental implications of greigite (Fe3S4) formation from Hole U1433A of the IODP Expedition 349, South China Sea. Marine Geology 394, 82–97.

Ducassou, E., Fournier, L., Sierro, F.J., Alvarez Zarikian, C.A., Lofi, J., Flores, J.A., Roque, C., 2016. Origin of the large Pliocene and Pleistocene debris flows on the Algarve margin. Marine Geology 377, 58–76.

Dunlop, D., Özdemir, Ö., 1997. Rock magnetism: fundamentals and frontiers. Cambridge Studies in Magnetism Series.

Ercilla, G., Juan, C., Hernández-Molina, J., Bruno, M., Estrada, F., Alonso, B., Casas, D., Farran, M., Llave, E., García, M., Vázquez, J., D'Acremont, E., Gorini, C., Palomino, D., Valencia, J., El Moumni, B., Ammar, A., 2016. Significance of bottom currents in deep-sea morphodynamics: an example from the Alboran Sea. Marine Geology 378, 157–170.

Evans, M., Heller, F., 2003. Environmental Magnetism: Principles and Applications of Enviromagnetics (San Diego, California).

Eynaud, F., de Abreu, L., Voelker, A., Schönfeld, J., Salgueiro, E., Turon, J.-L., Penaud, A., Toucanne, S., Naughton, F., Sánchez Goñi, M., Malaizé, B., Cacho, I., 2009. Position of the Polar Front along the western Iberian margin during key cold episodes of the last 45 ka. Geochemistry, Geophysics, Geosystems 10. https://doi.org/10.1029/2009GC002398.

Faugères, J.-C., Stow, D., 1993. Bottom-current-controlled sedimentation: a synthesis of the contourite problem. Sedimentary Geology 82, 287–297.

Faugères, J.-C., Gonthier, E., Stow, D., 1984. Contourite drift molded by deep Mediterranean Outflow. Geology 12, 296–300.

Faugères, J.-C., Stow, D., Imbert, P., Viana, A., 1999. Seismic features diagnostic of contourite drifts. Marine Geology 162, 1–38.

GEBCO Digital Atlas, 2003. British Oceanographic Data Centre on Behalf of IOC and IHO.

Gonthier, E., Faugères, J.-C., Stow, D., 1984. Contourite facies of the Faro Drift, Gulf of Cadiz. In: Stow, D., Piper, D. (Eds.), Fine Grained Sediments, Deepwater Processes and Facies. Special Publication. Geological Society, London, pp. 275–291.

Govin, A., Holzwarth, U., Heslop, D., Keeling, L., Zabel, M., Mulitza, S., Collins, J., Chiessi, C., 2012. Distribution of major elements in Atlantic surface sediments (36°N - 49°S): imprint of terrigenous input and continental weathering. Geochemistry Geophysics Geosystems 13. https://doi.org/10.1029/2011GC003785.

Hernández-Molina, F.J., Somoza, L., Vázquez, J.T., Lobo, F., Fernández-Puga, M.C., Llave, E., Díaz del Río, V., 2002. Quaternary stratigraphic stacking patterns on the continental shelves of the southern Iberian Peninsula: their relationship with global climate and palaeoceanographic changes. Quaternary International 92, 5–23.

Hernández-Molina, J., Llave, E., Somoza, L., Fernández-Puga, M.C., Maestro, A., León, R., Medialdea, T., Barnolas, A., García, M., Díaz del Río, V., Fernández-Salas, L.M., Vázquez, J.T., Lobo, F., Alveirinho Dias, J.M., Rodero, J., Gardner, J., 2003. Looking for clues to palaeoceanographic imprints: a diagnosis of the Gulf of Cádiz contourite depositional systems. Geology 31, 19–22.

Hernández-Molina, J., Llave, E., Stow, D., García, M., Somoza, L., Vázquez, J., Lobo, F., Maestro, A., Díaz del Río, V., Léon, R., Medialdea, T., Gardner, J., 2006. The contourite depositional system of the Gulf of Cadiz: a sedimentary model related to the bottom current activity of the Mediterranean outflow water and its interaction with the continental margin. Deep-Sea Research 53, 1420–1463.

Hernández-Molina, F.J., Paterlini, M., Violante, R., Marshall, P., de Isasi, M., Somoza, L., Rebesco, M., 2009. Contourite depositional system on the Argentine slope: an exceptional record of the influence of Antarctic water masses. Geology 37, 507–510.

Hernández-Molina, F.J., Serra, N., Stow, D., Llave, E., Ercilla, G., Van Rooij, D., 2011. Alongslope oceanographic processes and sedimentary products around the Iberian margin. Geo-Marine Letters 31, 315–341.

Hernández-Molina, F.J., Stow, D., Alvarez-Zarikian, C., Scientists, E.I., 2013. IODP Expedition 339 in the Gulf of Cadiz and off West Iberia: decoding the environmental significance of the Mediterranean outflow water and its global influence. Scientific Drilling 16, 1–11.

Hernández-Molina, F.J., Ercilla, G., Casas, D., MOWER team, 2014a. Rasgos erosivos y depósitos arenosos generados por la MOW alrededor de iberia: implicaciones paleoceanográficas, sedimentarias y económicas. MOWER – Informe Científico de campaña oceanográfica MOWER.

Hernández-Molina, F.J., Stow, D., Alvarez-Zarikian, C., Acton, G., Bahr, A., Balestra, B., Ducassou, E., Flood, R., Flores, J., Furota, S., Grunert, P., Hodell, D., Jimenez-Espejo, F., Kim, J., Krissek, L., Kuroda, J., Li, B., Llave, E., Lofi, J., Lourens, L., Miller, M., Nanayama, F., Nishida, N., Richter, C., Roque, C., Pereira, H., Sanchez Goñi, M., Sierro, F., Singh, A., Sloss, C., Takashimizu, Y., Tzanova, A., Voelker, A., Williams, T., Xuan, C.,

2014b. Onset of Mediterranean Outflow into the North Atlantic. Science 344, 1244–1250.
Hernández-Molina, F.J., Sierro, F., Llave, E., Roque, C., Stow, D., Williams, T., Lofi, J., Van der Schee, M., Arnáiz, A., Ledesma, S., Rosales, C., Rodríguez-Tovar, F., Pardo-Igúzquiza, E., Brackenridge, R., 2016. Evolution of the gulf of Cadiz margin and southwest Portugal contourite depositional system: tectonic, sedimentary and paleoceanographic implications from IODP expedition 339. Marine Geology 377, 7–39.
Hrouda, F., Chlupáčová, J., Pokorný, J., 2006. Low-field variation of magnetic susceptibility measured by the KLY-4S Kappabridge and KLF-4A magnetic susceptibility meter: accuracy and interpretational programme. Studia Geophysica et Geodaetica 50, 283–299.
Juan, C., Ercilla, G., Hernández-Molina, J., Estrada, F., Alonso, B., Casas, D., García, M., Farran, M., Llave, E., Palomino, D., Vázquez, J., Medialdea, T., Gorini, C., D'Acremont, E., El Moumni, B., Ammar, A., 2016. Seismic evidence of current-controlled sedimentation in the Alboran Sea during the Pliocene and Quaternary: palaeoceanographic implications. Marine Geology 378, 292–311.
Kaboth, S., Bahr, A., Reichart, G.-J., Jacobs, B., Lourens, L., 2016. New insights into upper MOW variability over the last 150 kyr from IODP 339 Site U1386 in the Gulf of Cadiz. Marine Geology 377, 136–145.
Kaboth, S., de Boer, B., Bahr, A., Zeeden, C., Lourens, L., 2017a. Mediterranean Outflow Water dynamics during the past ~570 kyr: regional and global implications. Paleoceanography 32, 634–647.
Kaboth, S., Grunert, P., Lourens, L., 2017b. Mediterranean Outflow Water variability during the Early Pleistocene. Climate of the Past 13, 1023–1035.
Knutz, P., 2008. Paleoceanographic significance of contourite drifts. In: Rebesco, M., Camerlenghi, A. (Eds.), Contourites. Developments in Sedimentology vol. 60. Elsevier, Amsterdam, pp. 511–535.
Laberg, J., Camerlenghi, A., 2008. The significance of contourites for submarine slope stability. In: Rebesco, M., Camerlenghi, A. (Eds.), Contourites. Developments in Sedimentology vol. 60. Elsevier, Amsterdam, pp. 537–556.
Lebreiro, S., Moreno, J., McCave, I.N., Weaver, P., 1996. Evidence for Heinrich layers off Portugal (Tore Seamount: 39N, 12W). Marine Geology 131, 47–56.
Lebreiro, S., Voelker, A., Vizcaino, A., Abrantes, F., Alt-Epping, U., Jung, S., Thouveny, N., Gràcia, E., 2009. Sediment instability on the Portuguese continental margin under abrupt glacial climate changes (last 60 kyr). Quaternary Science Reviews 28, 3211–3223.
Lee, H., Syvitski, J., Parker, G., Orange, D., Locat, J., Hutton, E., Imran, J., 2002. Distinguishing sediment waves from slope failure deposits: field examples, including the 'Humboldt slide', and modelling results. Marine Geology 192, 79–104.
Liu, Q., Roberts, A., Larrasoaña, J., Banerjee, S., Guyodo, Y., Tauxe, L., Oldfield, F., 2012. Environmental magnetism: principles and applications. Reviews of Geophysics 50. https://doi.org/10.1029/2012RG000393.
Llave, E., Hernández-Molina, F.J., Somoza, L., Díaz del Río, V., Stow, D., Maestro, A., Alveirinho Dias, J.M., 2001. Seismic stacking pattern of the Faro-Albufeira contourite system (Gulf of Cádiz): a Quaternary record of paleoceanographic and tectonic influences. Marine Geophysics Research 22, 487–508.
Llave, E., Schönfeld, J., Hernández-Molina, F.J., Mulder, T., Somoza, L., del Rio, V.D., Sanchez-Almazo, I., 2006. High-resolution stratigraphy of the Mediterranean outflow contourite system in the Gulf of Cadiz during the late Pleistocene: the impact of Heinrich event. Marine Geology 227, 241–262.
Llave, E., Hernández-Molina, J., Somoza, L., Stow, D., Díaz Del Río, V., 2007. Quaternary evolution of the contourite depositional system in the Gulf of Cádiz. In: Viana, A., Rebesco, M. (Eds.), Economic and Paleoceanographic Importance of Contourites. Geological Society of London, Special Publication vol. 276, pp. 49–79.
Llave, E., Hernández-Molina, F.J., García, M., Ercilla, G., Roque, C., Juan, C., Mena, A., Preu, B., Rooij, D., Rebesco, M., Brackenridge, R., Jané, G., Gómez-Ballesteros, M., Stow, D., 2019. Contourites along the Iberian continental margins: conceptual and economic implications. In: McClay, K., Hammerstein, J. (Eds.), Passive Margins: Tectonics, Sedimentation and Magmatism. Geological Society London Special Publications, pp. 403–436.
Magill, C., Ausín, B., Wenk, P., McIntyre, C., Skinner, L., Martínez-García, A., Hodell, D., Haug, G., Kenney, W., Eglinton, T., 2018. Transient hydrodynamic effects influence organic carbon signatures in marine sediments. Nature Communications 9. https://doi.org/10.1038/s41467-018-06973-w.
McCave, I.N., 2001. Nepheloid layers. In: Steele, J., Thorpe, S., Turekian, K. (Eds.), Encyclopedia of Ocean Sciences. Academic Press, London, pp. 1861–1870.
Mena, A., Francés, G., Pérez-Arlucea, M., Hanebuth, T., Bender, V., Nombela, M., 2018. Evolution of the Galicia Interior Basin over the last 60 ka: sedimentary processes and palaeoceanographic implications. Journal of Quaternary Science 33, 536–549.
Miramontes, E., Garreau, P., Caillaud, M., Jouet, G., Pellen, R., Hernández-Molina, F.J., Clare, M.A., Cattaneo, A., 2019. Contourite distribution and bottom currents in the NW Mediterranean Sea: coupling seafloor geomorphology and hydrodynamic modelling. Geomorphology 333, 43–60.
Naughton, F., Sanchez Goñi, M., Rodrigues, T., Salgueiro, E., Costas, S., Desprat, S., Duprat, J., Michel, E., Rossignol, L., Zaragosi, S., Voelker, A., Abrantes, F., 2016. Climate variability across the last deglaciation in NW Iberia and its margin. Quaternary International 414, 9–22.
Nelson, C., Baraza, J., Maldonado, A., 1993. Mediterranean undercurrent sandy contourites, Gulf of Cadiz, Spain. Sedimentary Geology 82, 103–131.
Ohkouchi, N., Eglinton, T., Keigwin, L., Hayes, J., 2002. Spatial and temporal offsets between proxy records in a sediment drift. Science 298, 1224–1227.
O'Reilly, W., 1984. Rock and Mineral Magnetism. https://doi.org/10.1007/978-1-4684-8468-7 (Glasgow).
Pinheiro, L., Wilson, R., Pena dos Reis, R., Whitmarsh, R., Ribeiro, A., 1996. The Western Iberia Margin: a geophysical and geological overview. In: Whitmarsh, R., Sawyer, D., Klaus, A., Masson, D. (Eds.), Proceedings of the Ocean Drilling Program, Scientific Results, pp. 3–23.
Pollard, S., Griffiths, C.R., Cunningham, S.A., Read, J.F., Perez, F.F., Ríos, A.F., 1996. Vivaldi 1991 - a study of the formation, circulation and ventilation of Eastern North Atlantic Central Water. Progress in Oceanography 37, 167–192.
Pomar, L., Morsilli, M., Hallock, P., Bádenas, B., 2012. Internal waves, an under-explored source of turbulence events in the sedimentary record. Earth Sciences Reviews 111, 56–81.
Preu, B., Hernández-Molina, F.J., Violante, R., Piola, A.R., Paterlini, C.M., Schwenk, T., Voigt, I., Krastel, S., Spiess, V., 2013. Morphosedimentary and hydrographic features of the northern Argentine margin: the interplay between erosive, depositional and gravitational processes and its conceptual implications. Deep-Sea Research. Part I: Oceanographic Research Papers 75, 157–174.
Rasmussen, S., Lykke-Andersen, H., Kuijpers, A., Troelstra, S.R., 2003. Post-Miocene sedimentation at the continental rise of Southeast Greenland: the interplay between turbidity and contour currents. Marine Geology 196, 37–52.
Rasmussen, S., Bigler, M., Blockley, S.P., Blunier, T., Buchardt, S.L., Clausen, H.B., Cvijanovic, I., Dahl-Jensen, D., Johnsen, S.J., Fischer, H., Gkinis, V., Guillevic, M., Hoek, W.Z., Lowe, J.J., Pedro, J.B., Popp, T., Seierstad, I.K., Steffensen, J.P., Svensson, A.M., Vallelonga, P., Vinther, B.M., Walker, M.J.C., Wheatley, J.J., Winstrup, M., 2014. A stratigraphic framework for abrupt climatic changes during the Last Glacial period based on three synchronized Greenland ice-core records: refining and extending the INTIMATE event stratigraphy. Quaternary Science Reviews 106, 14–28.
Rebesco, M., Hernández-Molina, F.J., Van Rooij, D., Wåhlin, A., 2014. Contourites and associated sediments controlled by deep-water circulation processes: state-of-the-art and future considerations. Marine Geology 352, 111–154.
Reimer, P., Bard, E., Bayliss, A., Beck, J., Blackwell, P., Bronk Ramsey, C., Grootes, P., Guilderson, T., Haflidason, H., Hajdas, I., Hattz, C., Heaton, T., Hoffmann, D., Hogg, A., Hughen, K., Kaiser, K., Kromer, B., Manning, S., Niu, M., Reimer, R., Richards, D., Scott, E., Southon, J., Staff, R, Turney, C., van der Plicht, J., 2013. IntCal13 and Marine13 Radiocarbon Age calibration curves 0–50,000 years cal BP. Radiocarbon 55, 1869–1887.
Rey, D., López-Rodríguez, N., Rubio, B., Vilas, F., Mohamed, K., Pazos, O., Bógalo, M., 2000. Magnetic properties of estuarine-like sediments: the study case of the Galician Rias. Journal of Iberian Geology 26, 151–170.
Rey, D., Mohamed, K., Bernabeu, A., Rubio, B., Vilas, F., 2005. Early diagenesis of magnetic minerals in marine transitional environments: geochemical signatures of hydrodynamic forcing. Marine Geology 215, 215–236.
Rey, D., Álvarez-Iglesias, P., Araújo, M., Bernabeu, A.M., Comas, M., DeCastro, M., Druet, M., Ferreira da Silva, E., Ferrín, A., Gesteira, M., Martins, V., Mohamed, K., Rubio, B., Vilas, F., 2014. The NW Iberian continental shelf. In: Chiocci, F., Chivas, A. (Eds.), Continental Shelves of the World: Their Evolution During the Last Glacio-Eustatic Cycle. Geological Society, London, Memoirs vol. 41, pp. 91–108.
Roberts, A., 2015. Magnetic mineral diagenesis. Earth Science Reviews 151, 1–47.
Rodrigues, S., 2017. Seismostratigraphic Model of the Sines Contourite Drift (SW Portuguese Margin) - Depositional Evolution, Structural Control and Palaeoceanographic Implications. University of Lisbon, Lisbon (Msc Thesis).
Rogerson, M., Rohling, E.J., Weaver, P.P.E., Murray, J.W., 2005. Glacial to interglacial changes in the settling depth of the Mediterranean Outflow plume. Paleoceanography 20. https://doi.org/10.1029/2004PA001106.
Rogerson, M., Bigg, G., Rohling, E., Ramirez, J., 2012. Vertical density gradient in the eastern North Atlantic during the last 30,000 years. Climate Dynamics 39, 589–598.
Roque, C., Duarte, H., Terrinha, P., Valadares, V., Noiva, J., Cachão, M., Ferreira, J., Legoinha, P., Zitellini, N., 2012. Pliocene and Quaternary depositional model of the Algarve margin contourite drifts (Gulf of Cadiz, SW Iberia): seismic architecture, tectonic control and paleoceanographic insights. Marine Geology 303-306, 42–62.
Roque, C., Hernández-Molina, F.J., Ercilla, G., Casas, D., Quartau, R., Llave, E., Alonso, B., Ferran, M., Mena, A., Francés, G., Party, M.C., 2015. Slope failure and mass movements in the Sines Contourite Drift (West Portuguese Margin): preliminary results. VII Symposium MIA15, Malaga, Spain, pp. 579–581.
Salgueiro, E., Naughton, F., Voelker, A., Abreu, L., Alberto, A., Rossignol, L., Duprat, J., Magalhães, V., Vaqueiro, S., Turone, J.-L., Abrantes, F., 2014. Past circulation along the western Iberian margin: a time slice vision from the Last Glacial to the Holocene. Quaternary Science Reviews 106, 316–329.
Sánchez Goñi, M., Llave, E., Oliveira, D., Naughton, F., Desprat, S., Ducassou, E., Hodell, D., Hernández-Molina, F.J., 2016. Climate changes in south western Iberia and Mediterranean Outflow variations during two contrasting cycles of the last 1 Myrs: MIS 31–MIS 30 and MIS 12–MIS 11. Global and Planetary Change 136, 18–29.
Schlitzer, R., 2018. Ocean Data View. http://odv.awi.de.
Schönfeld, J., Zahn, R., 2000. Late Glacial to Holocene history of the Mediterranean Outflow. Evidence from benthic foraminiferal assemblages and stable isotopes at the Portuguese margin. Palaeogeography. Palaeoclimatology. Palaeoecology 159, 85–111.
Schönfeld, J., Erlenkeuser, H., Zahn, R., 1993. Stratigraphy: preliminary results of piston core SO75 26KL. In: Kudrass, H. (Ed.), SONNE CRUISE SO-75-3: Cruise Report 1992. Test of the Geological Equipment by Surveying and Sampling of the Southwestern Portuguese Continental Slope and the Ampere Seamount. Bundesanst. Geowiss. Rohstoffe, Hannover, pp. 97–99.
Serra, N., Ambar, I., 2002. Eddy generation in the Mediterranean undercurrent. Deep-Sea Research II 49, 4225–4243.
Shanmugam, G., 2016. Slides, Slumps, Debris Flows, Turbidity Currents, and Bottom Currents. Reference Module in Earth Systems and Environmental Sciences. https://doi.org/10.1016/B978-0-12-409548-9.04380-3.
Siddall, M., Rohling, E., Thompson, G., Waelbroeck, C., 2008. Marine isotope stage 3 sea level fluctuations: data synthesis and new outlook. Reviews of Geophysics, RG4003 https://doi.org/10.1029/2007RG000226.
Silva, P., Roque, C., Drago, T., Alonso, B., Henry, B., Ercilla, G., Lopes, A., López-González, N., Casas, D., Naughton, F., Vázquez, J., 2020. Multidisciplinary characterization of

Quaternary mass movement deposits in the Portimão Bank (Gulf of Cadiz, SW Iberia). Marine Geology 420. https://doi.org/10.1016/j.margeo.2019.106086.
Stow, D., Faugères, J., 2008. Contourite facies and the facies model. In: Rebesco, M., Camerlenghi, A. (Eds.), Contourites. Developments in Sedimentology vol. 60. Elsevier, pp. 223–256.
Stow, D., Hernández-Molina, J., Alvarez-Zarikian, C., Scientists, E., 2013. Expedition 339 summary. In: IODP (Ed.), Proceedings of the Integrated Ocean Drilling Program, p. 339. https://doi.org/10.2204/iodp.proc.339.101.2013.
Stríkis, N.M., Cruz, F.W., Barreto, E.A.S., Naughton, F., Vuille, M., Cheng, H., Voelker, A.H.L., Zhang, H., Karmann, I., Edwards, R.L., Auler, A.S., Santos, R.V., Sales, H.R., 2018. South American monsoon response to iceberg discharge in the North Atlantic. In: Broecker, W. (Ed.)Proceedings of the National Academy of Sciences of the United States of America vol. 115, pp. 3788–3793.
Talley, L., McCartney, M., 1982. Distribution and circulation of Labrador Sea water. Journal of Physical Oceanography 12, 1189–1205.
Taylor, A., Goldring, R., 1993. Description and analysis of bioturbation and ichnofabric. Journal of the Geological Society of London 150, 141–148.
Teixeira, M., Terrinha, P., Roque, C., Rosa, M., Ercilla, G., Casas, D., 2019. Interaction of alongslope and downslope processes in the Alentejo Margin (SW Iberia) – implications on slope stability. Marine Geology 410, 88–108.
Terrinha, P., Pinheiro, L., Henriet, J., Matias, L., Ivanov, M., Monteiro, J., Akhmetzhanov, A., Volkonskaya, A., Cunha, T., Shaskin, P., Rovere, M., 2003. Tsunamigenic–seismogenic structures, neotectonics, sedimentary processes and slope instability on the southwest Portuguese Margin. Marine Geology 195, 55–73.
Terrinha, P., Kullberg, J., Neres, M., Alves, T., Ramos, A., Ribeiro, C., Mata, J., Pinheiro, L., Afilhado, A., Matias, L., Luís, J., Anton Muñoz, J., Fernández, O., 2019a. Rifting of the Southwest and West Iberia continental margins. In: Quesada, C., Oliveira, J. (Eds.), The Geology of Iberia: A Geodynamic Approach. Regional Geology Reviews. Springer Nature, Switzerland, pp. 251–283.
Terrinha, P., Ramos, A., Neres, M., Valadares, V., Duarte, J., Martínez-Loriente, S., Silva, S., Mata, J., Kullberg, J., Casas-Sainz, A., Matias, L., Fernández, O., Anton Muñoz, J., Ribeiro, C., Font, E., Neves, C., Roque, C., Rosas, F., Pinheiro, L., Bartolomé, R., Sallarès, V., Magalhães, V., Medialdea, T., Somoza, L., Gràcia, E., Hensen, C., Gutscher, M.A., Ribeiro, A., Zitellini, N., 2019b. The Alpine orogeny in the West and Southwest Iberia Margins. In: Quesada, C., Oliveira, J. (Eds.), The Geology of Iberia: A Geodynamic Approach. Regional Geology Reviews, pp. 487–505.
Toucanne, S., Mulder, T., Schöenfeld, J., Hanquiez, V., Gonthier, E., Duprat, J., Cremer, M., Zaragosi, S., 2007. Contourites of the Gulf of Cadiz: a high-resolution record of the paleocirculation of the Mediterranean outflow water during the last 50,000 years. Palaeogeography, Palaeoclimatology, Palaeoecology 246, 354–366.
van Aken, H., 2000a. The hydrography of the mid-latitude Northeast Atlantic Ocean. I: the deep water masses. Deep-Sea Research I 47, 757–788.
van Aken, H., 2000b. The hydrography of the mid-latitude Northeast Atlantic Ocean. II: the intermediate water masses. Deep-Sea Research I 47, 789–824.
Venuti, A., Florindo, F., Michel, E., Hall, I., 2007. Magnetic proxy for the deep (Pacific) western boundary current variability across the mid-Pleistocene climate transition. Earth and Planetary Science Letters 259, 107–118.
Voelker, A., Lebreiro, S., Schönfeld, J., Cacho, I., Erlenkeuser, H., Abrantes, F., 2006. Mediterranean outflow strengthening during northern hemisphere coolings: a salt source for the glacial Atlantic? Earth and Planetary Science Letters 245, 39–55.
Yamamoto, M., Yamamuro, M., Tada, R., 2000. Late Qyaternary records of roganic carbon, calcium carbonate, and biomarkersform the Site 1016 off Point Conception, California margin. In: Lyle, M., Koizumi, I., Richter, C., Moore Jr., T. (Eds.), Proceedings of the Ocean Drilling Program, Scientific Results, pp. 183–194.
Zahn, R., Schönfeld, J., Kudrass, H., Park, M., Erlenkeuser, H., Grootes, P., 1997. Thermohaline Instability in the North Atlantic during melt water events: stable isotope and ice-rafted detritus records from core SO07-26KL, Portuguese margin. Paleoceanography 12, 696–710.
Zenk, W., Armi, L., 1990. The complex spreading pattern of Mediterranean water off the Portuguese continental slope. Deep-Sea Research 37, 1805–1823.
Zitellini, N., Mendes, L.A., Cordoba, D., Danobeitia, J., Nichols, R., Pellis, G., Ribeiro, A., Sartori, R., Torelli, L., Bartolome, R., Bortoluzzi, G., Calafato, A., Carrilho, F., Casoni, L., Chierici, F., Corela, C., Correggiari, A., Vedova, B., Gràcia, E., Jornet, P., Landuzzi, M., Ligi, M., Magagnoli, A., Marozzi, G., Matias, L., Penitenti, D., Rodriguez, P., Rovere, M., Terrinha, P., Vigliotti, L., Ruiz, A., 2001. Source of 1755 Lisbon earthquake and tsunami investigated. Eos, Transactions American Geophysical Union 82, 285–296.
Zitellini, N., Gràcia, E., Matias, L., Terrinha, P., Abreu, M., DeAlteriis, G., Henriet, J.P., Dañobeitia, J., Masson, D., Mulder, T., Ramella, R., Somoza, L., Diez, S., 2009. The quest for the Africa-Eurasia plate boundary west of the Strait of Gibraltar. Earth and Planetary Science Letters 280, 13–50.